Check for updates

JGR Atmospheres

RESEARCH ARTICLE
10.1029/2026JD047500

Special Collection:
Advances in Earth's Energy Balance, Aerosols, Cloud Processes & Climate

Moisture Aggregation and the Cloud Transition Zone Shape Mesoscale Aerosol Properties

Eshkol Eytan[1,2,3], Martin Wirth[4], Silke Groß[4], J. Christine Chiu[5], and Graham Feingold[1]

[1]NOAA Chemical Sciences Laboratory, Boulder, CO, USA, [2]Cooperative Institute for Research in Environmental Sciences, Boulder, CO, USA, [3]Now at the Department of Earth and Environmental Sciences, Ben-Gurion University of the Negev, Be'er-Sheva, Israel, [4]Institut für Physik der Atmosphäre, Deutsches Zentrum für Luft- und Raumfahrt, Oberpfaffenhofen, Germany, [5]Department of Atmospheric Science, Colorado State University, Fort Collins, CO, USA

Abstract Mesoscale moisture aggregation and cloud organization in shallow convection have gained much attention regarding their role in Earth's energy budget and cloud feedbacks on climate. Because aerosol particles swell in humid air, mesoscale moisture patterns are expected to be accompanied by corresponding variations in aerosol optical depth (AOD). However, observing such patterns is challenging because space-borne imagers cannot reliably retrieve AOD in the aerosol–cloud transition zone (CTZ), where radiative transfer is different from both clear-sky and cloudy conditions. By linking the concepts of moisture aggregation and the CTZ, we ask whether mesoscale patterns organize AOD patterns on the mesoscale, and what are the structures and components of the CTZ in different cloud morphologies. We address these questions using space-borne images complemented by high-resolution airborne LiDAR acquired during the EUREC^{4}A field campaign, which sampled a range of cloud patterns and aerosol concentrations. We show that small cumulus clouds contribute to the CTZ through local moistening of the cloud layer. As moisture aggregates to support larger clouds, thin detrained layers near the trade-wind inversion spread at the top of the cloud layer over tens of kilometers and increase AOD while often manifesting as optically thin clouds that would often not be detected by satellites. Such perturbations reverse during dust events, when precipitation-processed air is cleaner than the background aerosol profile. Our results indicate that expected mesoscale AOD gradients are missing from satellite retrievals and suggest that mesoscale dynamics affect Earth's energy budget through shaping aerosol-cloud-radiation interactions.

Plain Language Summary Atmospheric science often treats the sky as either "cloudy" or "clear," despite a broad transition zone between clouds and cloud-free air. In this transition zone, which covers about half of the cloud-free sky over the ocean, microscopic particles (aerosols) interact with moisture and nearby clouds, increasing the amount of sunlight reflected to space and introducing biases in satellite observations. Recent studies show that shallow tropical clouds frequently organize into large-scale patterns that can influence Earth's climate. Here, we combine satellite imagery with high-resolution, aircraft-based observations to understand how cloud organization shapes the aerosol-cloud transition zone. We find that the humidity around small clouds locally enhances reflected sunlight by allowing aerosols to swell, and by producing faint clouds that often go undetected. When clouds organize into larger structures, thin hazy layers spread far from cloud tops, increasing reflected sunlight in different ways. These effects reverse during dust events, when precipitating clouds remove aerosols, leaving cloud-influenced air cleaner than the surrounding environment. Overall, our results demonstrate that atmospheric flows that organize clouds also shape aerosols and their radiative effect, therefore improving our understanding of aerosol-cloud-radiation interactions, which are important processes in Earth's energy budget that drive the largest uncertainties in climate projections.

Key Points:

- Mesoscale features of the aerosol–cloud transition zone are revealed across cloud patterns in combined satellite and airborne observations
- Dynamics of moisture aggregation and cloud patterns influence cloud-free optical properties, depending on background aerosol conditions
- Results advocate linking mesoscale dynamics to aerosol–cloud–radiation interactions research to better understand Earth's energy budget

Supporting Information:

Supporting Information may be found in the online version of this article.

Correspondence to:

E. Eytan,
eytane@bgu.ac.il

Citation:

Eytan, E., Wirth, M., Groß, S., Chiu, J. C., & Feingold, G. (2026). Moisture aggregation and the cloud transition zone shape mesoscale aerosol properties. *Journal of Geophysical Research: Atmospheres*, *131*, e2026JD047500. https://doi.org/10.1029/2026JD047500

Received 12 MAY 2026
Accepted 16 OCT 2026

Author Contributions:

Conceptualization: Eshkol Eytan
Data curation: Martin Wirth, Silke Groß
Formal analysis: Eshkol Eytan
Funding acquisition: J. Christine Chiu, Graham Feingold
Investigation: Eshkol Eytan, Graham Feingold

© 2026 The Author(s). Journal of Geophysical Research: Atmospheres published by Wiley Periodicals LLC on behalf of American Geophysical Union. This is an open access article under the terms of the Creative Commons Attribution License, which permits use, distribution and reproduction in any medium, provided the original work is properly cited.

1. Introduction

Aerosol optical depth (AOD) is the most fundamental remote sensing retrieval of aerosol. It is used for a wide variety of studies that include estimates of aerosol radiative effects and their role in Earth's energy budget (Loeb & Manalo-Smith, 2005; Su et al., 2013; Thorsen et al., 2020; Yu et al., 2006), air pollution monitoring (Chang et al., 2014; Lee, 2020; Zhai et al., 2021), investigations of aerosol-cloud interactions (Andreae, 2009; Koren et al., 2010; Seinfeld et al., 2016), aerosol transport (e.g., smoke and dust), and links between biological activity and aerosol sources (Dror et al., 2018; Sellegri et al., 2024). On the operational side, AOD is used to compare

Methodology: Eshkol Eytan, Martin Wirth
Validation: Eshkol Eytan
Visualization: Eshkol Eytan
Writing – original draft: Eshkol Eytan
Writing – review & editing: Eshkol Eytan, Martin Wirth, Silke Groß, J. Christine Chiu, Graham Feingold

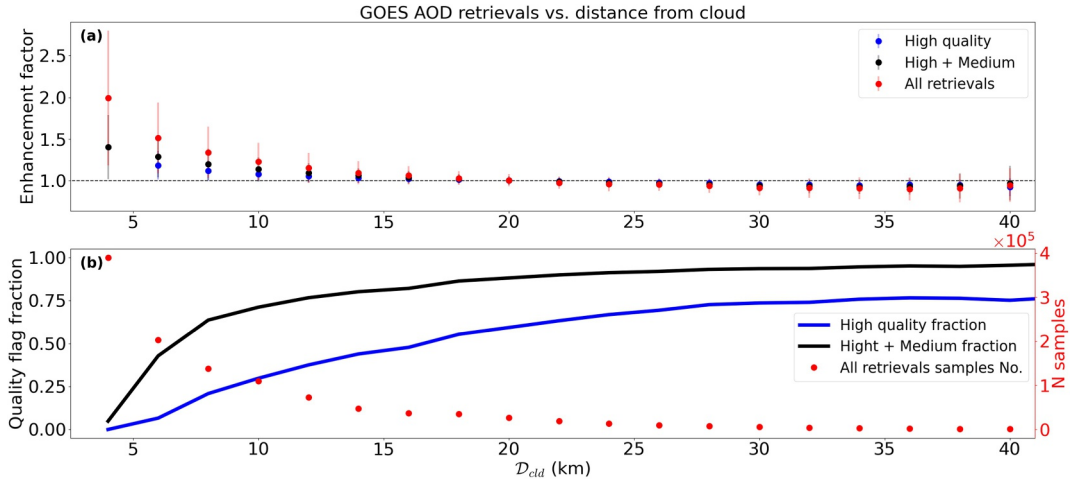

Figure 1. Aerosol optical depth (AOD) increase near clouds. Geostationary Operational Environmental Satellite-Advanced Baseline Imager retrievals of AOD as a function of distance from cloud for all analyzed days (Table 1). (a) Mean and standard deviation of AOD with distance from nearest cloud ($\mathcal{D}_{\text{cld}}$) for three quality levels: All retrieved pixels (red), medium and high quality (black), and only high quality (blue). (b) The fraction of high quality and medium + high quality for each $\mathcal{D}_{\text{cld}}$ bin. Red dots represent the number of samples in each $\mathcal{D}_{\text{cld}}$ bin. The analysis includes 242 images over the North Atlantic near Barbados (see Section 2.1), each covering 2° × 2° with a spatial resolution of 2 km. The enhancement factor is defined as the AOD of each pixel normalized by the background ("pure" clear-sky) AOD, calculated as the mean of all pixels far enough from clouds, where $\mathcal{D}_{\text{cld}} > 15$ km (Christensen et al., 2017; Eytan et al., 2025). This normalization allows us to analyze multiple days together despite the large day-to-day variability in aerosol loading.

models with observations (Liang & Griswold, 2025; Ma & Yu, 2015) and is assimilated in weather and reanalysis models (Garrigues et al., 2023; Randles et al., 2017).

Most of the above-mentioned studies have used AOD retrievals from passive sensors (i.e., multi-spectral imagers) onboard satellites, the advantage being that such data provide global coverage with large statistics and fairly detailed spatial information. A widely recognized caveat of AOD retrievals from passive sensors is their strong sensitivity to the presence of nearby clouds (Christensen et al., 2017; Marshak et al., 2021; Wen et al., 2006). These near-cloud areas are often referred to as the aerosol–cloud transition zone (CTZ), extending up to 10 km from cloud boundaries (Charlson et al., 2007; Koren et al., 2007; Várnai & Marshak, 2018). AOD retrievals within the CTZ from passive spaceborne instruments exhibit biases for several reasons:

1. *Cloud contamination*—pixels near detected cloud edges frequently contain undetected clouds whose extinction exceeds that of aerosols (Eytan et al., 2020; Hirsch et al., 2014; Mieslinger et al., 2022).
2. *3D radiative transfer*—Most AOD retrievals today use a 1D approximation for the radiative transfer, which breaks down near clouds (Wen et al., 2013; Yang et al., 2022).
3. *Modified aerosol size distributions*—AOD retrievals use aerosol size distribution models that are often based on measurements in drier conditions away from clouds, whereas aerosol near clouds undergo hygroscopic growth and cloud processing.

Active sensors such as LiDAR, while lacking broad spatial context and large statistics due to their narrow field of view, deliver sensitive measurements and vertical profiles that provide valuable insights into the CTZ (Eck et al., 2014; Hu et al., 2025; Ruiz de Morales et al., 2026).

Figure 1a shows the effect of the CTZ via the mean normalized AOD (i.e., enhancement factor) as a function of the Euclidean distance from the nearest cloudy pixel detected by GOES ($\mathcal{D}_{\text{cld}}$). The analysis was conducted for 242 images of the Geostationary Operational Environmental Satellite-Advanced Baseline Imager (GOES-ABI).

The different colors in Figure 1a represent pixels flagged with different retrieval quality, with red being all retrieved pixels and blue only the high-quality retrievals. The figure shows how AOD increases above background values, and how the different quality levels deviate when $\mathcal{D}_{\text{cld}} < 15$ km. This is consistent with Christensen et al. (2017), who analyzed AOD retrievals derived from different instruments. The red circles in

21698996, 2026, 21, Downloaded from https://agupubs.onlinelibrary.wiley.com/doi/10.1029/2026JD047500 by Dtsch Zentrum F. Luft-U. Raum Fahrt In D. Helmholtz Gemein., Wiley Online Library on [11/11/2026]. See the Terms and Conditions (https://onlinelibrary.wiley.com/terms-and-conditions) on Wiley Online Library for rules of use; OA articles are governed by the applicable Creative Commons License

21698996, 2026, 21, Downloaded from https://agupubs.onlinelibrary.wiley.com/doi/10.1029/2026JD047500 by Dtsch Zentrum F. Luft-U. Raum Fahrt In D. Helmholtz Gemein., Wiley Online Library on [11/11/2026]. See the Terms and Conditions (https://onlinelibrary.wiley.com/terms-and-conditions) on Wiley Online Library for rules of use; OA articles are governed by the applicable Creative Commons License

Figure 1b present the number of pixels in each distance bin, while the black and blue curves show the fraction of pixels belonging to each quality flag class.

As shown in Figure 1, the biases clouds exert on AOD retrievals force the algorithms to retrieve AOD with high confidence only at sufficiently large distances from clouds. Schwarz et al. (2017) showed that 20% of the pixels of the Moderate Resolution Imaging Spectroradiometer (MODIS) over the Atlantic Ocean are excluded from both cloud and aerosol retrievals because they do not satisfy the confidence requirements of either algorithm. Avoiding AOD retrievals within the CTZ introduces a sampling bias in aerosol spatial distribution, their estimated radiative effects, and their role in Earth's energy budget.

Recent studies have shown that the CTZ contributes substantially to non-cloudy fluxes at the top-of-atmosphere, underscoring its importance for Earth's energy budget (Eytan et al., 2025; Jahani et al., 2022; Twohy et al., 2009; Várnai & Marshak, 2014; Yang et al., 2022). Eytan et al. (2025) further demonstrated that the solar-spectrum radiative effect of the CTZ is comparable to the estimated clear-sky aerosol direct radiative effect within cloud fields, suggesting that aerosol radiative effects are strongly modulated (or even dominated) by the presence of clouds. This highlights the importance of the CTZ for understanding the role of aerosols in Earth's energy budget.

Two of the studies mentioned above (Eytan et al., 2020, 2025) also suggest that the CTZ includes multiple scales: small (cloud) scales and larger-scale gradients that are part of mesoscale patterns (see the first figure of each paper). Studies of the CTZ and its effects on remote sensing retrievals have historically focused on the cloud scale only, but more recent work by Rixen et al. (2025) suggests that the thermal radiative effect reported in Eytan et al. (2020) is related to mesoscale humid halos. Note that Eytan et al. (2020) reported that most of the effects occur up to 2–4 km away from clouds, indicating the dominance of cloud-scale gradients. Nevertheless, meso-scale cloud clustering tends to manifest as gradients in moisture and cloud density that should also yield mesoscale gradients in CTZ radiative effects.

Moisture aggregation on the mesoscale has been studied for decades, primarily in the context of deep convection (Tompkins, 2001). More recently, it has gained attention in shallow convection fields due to its strong relationship to trade-wind cloud organization and clustering (Bretherton & Blossey, 2017; Janssens et al., 2023; Narenpitak et al., 2021). The counterpart of moisture aggregation is the formation of large cloud-free voids, as moist regions become moister and dry regions become drier (Bretherton & Blossey, 2017). Such large dry patches should weaken the CTZ impact due to the absence of both clouds and excess humidity.

Considering the CTZ and moisture aggregation, this paper attempts to answer the questions: How do cloud and humidity aggregation affect AOD spatial distribution and retrievals? Can moisture aggregation explain the larger scales of the CTZ that were observed in Eytan et al. (2020, 2025)? Answering these questions is essential not only for mitigating CTZ-related retrieval biases, but also for improving our understanding of how aerosol–cloud–radiation interactions operate at the mesoscale.

To address these questions we use the Water Vapor LiDAR Experiment in Space (WALES) that was mounted on the High Altitude and Long Range Research Aircraft (HALO) during the EUREC^{4}A field campaign (ElUcidating the RolE of Cloud–Circulation Coupling in ClimAte). WALES profiles were co-located with GOES-ABI imagery and remote sensing products, to explore the effects of cloud aggregation on aerosol extinction spatial distribution and GOES AOD retrievals. While GOES imagery provides large-scale horizontal spatial information about the cloud field, the airborne LiDAR complements it with high-resolution and highly sensitive observations of ambient aerosol radiative properties and vertical profiles of humidity.

The paper is structured as follows: in Section 2, we present the data set and analysis methodology. In Section 3.1 we analyze satellite data to show the mesoscale gradients in radiative signal and AOD retrievals. In Section 3.2 and 3.3, we combine satellite imagery with airborne LiDAR to show how different cloud patterns and aerosol loading profiles affect the vertical structure of aerosol extinction along the mesoscale axes. In Section 4 we summarize and conclude the results.

21698996, 2026, 21, Downloaded from https://agupubs.onlinelibrary.wiley.com/doi/10.1029/2026JD047500 by Dtsch Zentrum F. Luft-U. Raum Fahrt In D. Helmholtz Gemein., Wiley Online Library on [11/11/2026]. See the Terms and Conditions (https://onlinelibrary.wiley.com/terms-and-conditions) on Wiley Online Library for rules of use; OA articles are governed by the applicable Creative Commons License

Table 1
Summary of the Days Analyzed in This Study

Date	Time (UTC)	Cloud patterns	Aerosol
28 Jan	15:20–20:40	Small Cu that deepened	Pristine
30 Jan	12:20–14:20	Small Cu and aggregated "Flowers"	Dusty at south-east
31 Jan	16:10–20:40	Small Cu with some Flowers	Dust layer at 2–3 km
02 Feb	12:30–19:10	Large Flowers	Heavy dust layer around 2.8 km
05 Feb	11:30–15:30	Flowers surrounded by small Cu (high cloud cover)	Diluted dust in the boundary layer
07 Feb	12:30–19:30	Large Flowers transitioned to small Cu	Pristine
09 Feb	11:00–15:30	Small Cu deepened to 4 km	High extinction with some dust
11 Feb	12:20–19:40	Deeper convection with 5 km tops	High extinction with some dust

2. Materials and Methods

2.1. The Data Set

2.1.1. The EUREC^{4}A Field Campaign

The EUREC^{4}A field campaign took place in the North Atlantic basin east of Barbados between January 20 and February 20, 2020 (Stevens et al., 2021). A pivotal role in EUREC^{4}A was played by the German research aircraft HALO (High Altitude and Long Range Research Aircraft), which flew at an altitude around 10 km while carrying a suite of remote-sensing instruments (Konow et al., 2021). During the field campaign, HALO conducted 15 flight days of approximately 8 hr each, mostly along a circular pattern centered at 13.3°N, 57.7°W, with an approximate diameter of 220 km.

With our focus on shallow clouds and their convective aggregation, we study only the 8 days that exhibited ideal shallow-convection conditions with no cirrus clouds. The analyzed days are summarized in Table 1.

2.1.2. WALES Airborne LiDAR

WALES (Water Vapor LiDAR Experiment in Space; Wirth et al. (2009)), which was mounted on the HALO aircraft, is a multi-wavelength differential absorption LiDAR that uses four high-resolution wavelengths in the 935 nm H_2O absorption band. WALES also includes a High Spectral Resolution LiDAR (HSRL) channel at 532 nm and depolarization channels at 1,064 nm and 532 nm for aerosol characterization. In this analysis, we mostly rely on the HSRL component at 532 nm.

WALES retrieves the aerosol backscatter ratio ($\beta_r = \beta/\beta_{\text{Rayleigh}}$) and the aerosol component of the two-way atmospheric transmittance (T^2_{aer}) at 1 Hz and with a vertical resolution of 15 m. β is the backscatter coefficient, and β_{Rayleigh} denotes the molecular backscatter alone. The sampling frequency corresponds to a horizontal resolution of roughly 200 m, given HALO's velocity of about 200 m s^{-1}. Aerosol extinction is retrieved using $\alpha_{\text{aer}} = -0.5\frac{dln\left(T^2_{\text{aer}}\right)}{dz}$, and smoothed to reduce the noisy data (see Text S2 in Supporting Information S1). On the vertical axis, smoothing is performed using a Savitzky-Golay first-order filter to compute the derivative, which results in a parabolic shape averaging kernel. A box filter is applied horizontally. All of the above result in an effective resolution of 5 km in the horizontal and 240 m in the vertical. The retrieved water vapor mixing-ratio profiles have an effective resolution of 2,500 and 200 m in the horizontal and vertical, respectively.

WALES also offers cloud retrievals at 40 m horizontal resolution at a 5 Hz sampling frequency (Wirth, 2021). These products are resampled to the β_r data resolution. Clouds are defined when there is a step in the 532 nm β_r profile exceeding 10; any 200 m sample with more than 0.2 cloud fraction was considered cloudy. Cloud-top height (CTH) is retrieved with an accuracy of 7.5 m. WALES is highly sensitive to optically thin clouds, which is a key advantage for this analysis. The retrieval of cloud optical depth at 532 nm (τ_{cld}) begins losing its accuracy when $\tau_{\text{cld}} > 3$; hence, above this value, the cloud can only be said to be optically thick. This is consistent with the definition of optically thin clouds in cumulus cloud fields (McCoy et al., 2023; Wood, Tseng, et al., 2018).

21698996, 2026, 21, Downloaded from https://agupubs.onlinelibrary.wiley.com/doi/10.1029/2026JD047500 by Dtsch Zentrum F. Luft-U. Raum Fahrt In D. Helmholtz Gemein., Wiley Online Library on [11/11/2026]. See the Terms and Conditions (https://onlinelibrary.wiley.com/terms-and-conditions) on Wiley Online Library for rules of use; OA articles are governed by the applicable Creative Commons License

2.1.3. GOES-16 ABI Imagery

While WALES contributes vertical profiling, high spatial resolution, and sensitive measurements, it lacks a broader spatial context due to its narrow, "pencil-like" field of view. This is where GOES-ABI imagery provides complementary information, offering a view of the surrounding cloud field in which the aircraft is flying, including cloud patterns, cloud field properties, and the aircraft's location relative to nearby clouds.

GOES-16 is a geostationary satellite carrying the Advanced Baseline Imager (ABI), which images the Earth's disk in 16 channels spanning the visible to longwave infrared, with a nadir spatial resolution of 0.5–1 km for solar wavelengths and 2 km for longwave channels (Schmit et al., 2005). In this study, we use the solar 0.86 μm channel together with the thermal 11.2 μm channel. Because the GOES-ABI solar channels have higher spatial resolution, the 0.86 μm channel is resampled to 2 km to match the resolution of the thermal channel. The imaging frequency used for the analysis is the full-disk scan that samples the target domain every 10 min.

This study uses GOES-derived AOD at 550 nm (AOD; Laszlo et al. (2008)) and CTH retrievals (ACHA product; Heidinger (2011a)), as well as the cloud mask (ACM product; Heidinger (2011b)). The cloud mask, with a spatial resolution of 2 km, defines a pixel as cloudy if the algorithm considers it confidently or probably cloudy. Trade wind cumulus clouds are often smaller than the native GOES resolution (Koren et al., 2008; Rodts et al., 2003), and so the cloud mask misses a significant number of these clouds. Hence, for sensitivity tests, we also developed an in-house cloud mask tuned for our specific region (see Text S1 in Supporting Information S1). The GOES CTH retrieval uses three thermal channels to infer cloud top temperature, which is converted to height using weather numerical model profiles (Heidinger et al., 2020). This product has a spatial resolution of 10 km and an uncertainty of 500 m. The AOD retrieval is based on the Moderate Resolution Imaging Spectroradiometer (MODIS) algorithm (Levy et al., 2013) and retrieves AOD at a resolution of 2 km with three quality flags: high, medium, and low.

2.2. Defining Convective Field Cores From Bi-spectral Imagery

The main goal of this study is to observe the structure and properties of the largest scales of the CTZ and examine how they vary across different cloud field patterns. To this end, we define a new distance metric that represents the distance from the nearest convective cores (D_{meso}). Our motivation for doing so is to focus on the *mesoscale* organization of water vapor, aerosols, and AOD. We assume that any convective field contains dominant, more intense convective cells that can be considered as the convective field cores (i.e., the center of mesoscale circulating flows; George et al. (2023)). In moist convection, these cores are expected to correspond to the brightest cloudy regions in the domain and to reach the highest altitudes. From a satellite perspective, such cores manifest as the most reflective pixels in the solar spectrum and the lowest brightness temperatures in the thermal infrared. We define convective cores as cloudy pixels that satisfy two criteria: a solar reflectance exceeding the 75th percentile of all cloudy pixels in the image, and a thermal signal lower than the 25th percentile of all cloudy pixels. These dynamic thresholds, based on the cloud radiance distributions within each image, ensure that the core definition is robust to variations in the diurnal cycle, environmental conditions, cloud patterns, and cloud fraction. As a result, convective cores are identified relative to the specific conditions present in each image. The domain size used to represent a cloud field in this analysis is $2^\circ \times 2^\circ$. This size was found to be optimal for the data set, as it is sufficiently large to capture mesoscale gradients (Orlanski, 1975) while small enough to avoid mixing different cloud patterns within a single image.

Figure 2 provides an illustrative example in the form of a GOES snapshot acquired on 5 February 2020 (05 February), a day characterized by aggregated clouds, which have recently been referred to as "Flowers" clouds (see Table 1). Figure 2a shows the solar 0.86 μm image and Figure 2b shows the corresponding thermal image. Applying the thresholds described above yields the convective-core mask that is shown in Figure 2c and used to compute the distance of each pixel to its nearest core pixel, defined as D_{meso} (Figure 2d). D_{meso} is the primary metric used throughout this study. Figure 2e shows an 8-min curtain of aerosol backscatter ratio (β_r) at 1,064 nm corresponding to the magenta aircraft trajectory shown in Figure 2a. Clouds are masked in white, and CTH and boundary layer top are indicated by a magenta and black dashed line, respectively. The timing of the GOES snapshot in Figure 2a is marked by a red star, which also indicates the location of HALO at that time. The corresponding curtain of water-vapor mixing ratio is shown in Figure 2f.

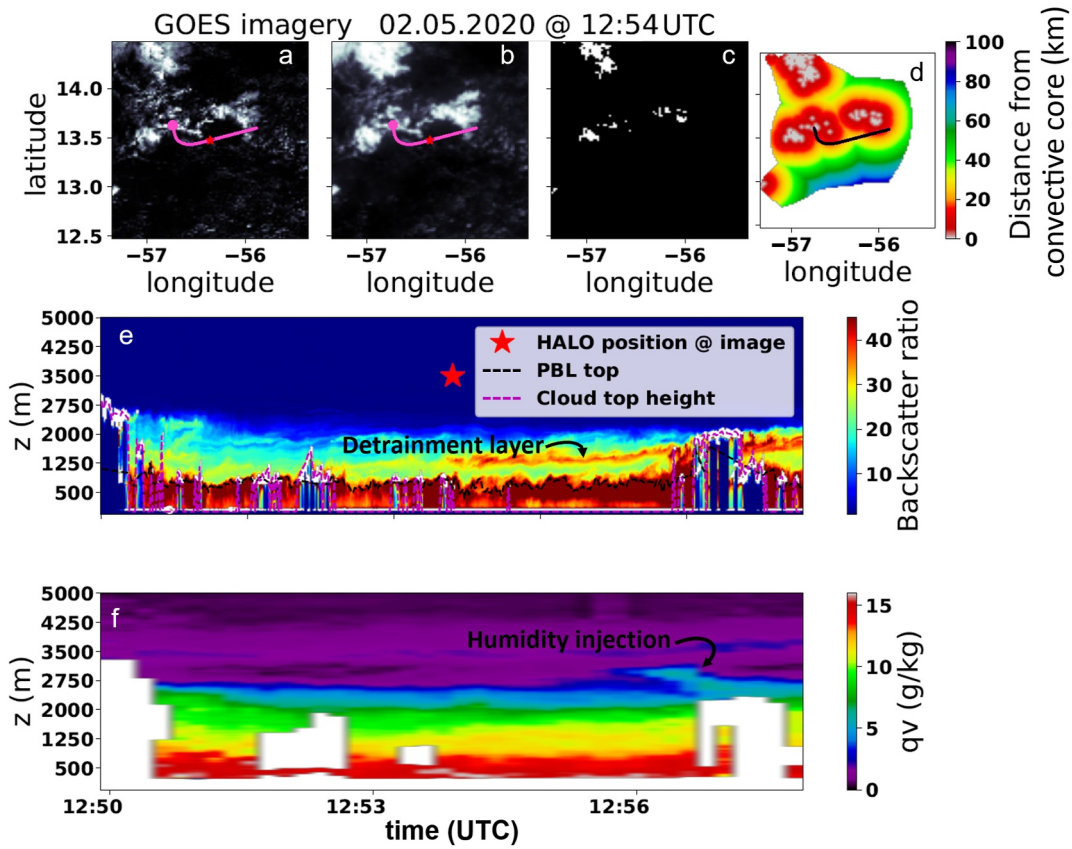

Figure 2. Visualization of the data set. Airborne LiDAR profiles of aerosol backscatter ratio at 1,064 nm and water vapor mixing ratio (panels e and f) co-located with GOES imagery (panels a, b; visible and thermal, respectively). The aircraft trajectory, marked by a magenta curve in the GOES images, begins at the magenta dot that marks the start of the time series in panels e, f. The red star in panels a, b represents the aircraft's location during image acquisition time (panels e, f). WALES retrievals of cloud-top height and planetary boundary layer top are marked by magenta and black dashed lines, respectively. The images in panels a, b are used to define the convective field cores (panel c), and the Euclidean distance from those pixels is calculated to get D_{meso} (panel d). This example, dominated by large aggregated clouds, is from the 5th of February 2020 at 12:54 UTC.

Figures 2a–2e show how HALO exits a large cloud, identified as a convective core, and approaches the edge of another. A detrainment layer is visible as a thin region of enhanced β_r extending away from the second cloud just below the inversion. The occurrence of such layers is examined throughout this study. Another interesting feature presented by this cloud is the vertical injection of moisture to higher altitudes (Figure 2f) where cyan-colored structures entrain into the drier (magenta) free troposphere. Figure 3 is similar to Figure 2 but for a different day (28 January) that was dominated by smaller, more sparse clouds. Notably, these clouds preferentially occupy certain regions of the scene, indicating that mesoscale organization is a persistent feature across cloud field types, and suggesting broad utility of D_{meso}.

Throughout the analysis, each 8-min pair of WALES LiDAR curtains (as in Figures 2 and 3) is paired with a GOES snapshot by selecting the HALO trajectory spanning 4 min before and after the image acquisition time, consistent with the 10-min GOES imaging frequency. This approach assumes that convective cores and the associated D_{meso} field remain approximately stationary over 4 min. Accordingly, each atmospheric column sampled by WALES is assigned the D_{meso} value of the corresponding GOES pixel in which the aircraft was positioned. Interpolation of the aircraft position across neighboring pixels is not applied as sensitivity tests showed that it does not affect the results.

D_{meso} is a pivotal metric in this study. It depends on the subjective definition of the convective cores and the binary mask that it produces (Figures 2c and 3c). The convective core mask depends on two main aspects of the analysis: (a) the percentile values used to define the dynamic thresholds of the cores; and (b) the applied cloud

21698996, 2026, 21, Downloaded from https://agupubs.onlinelibrary.wiley.com/doi/10.1029/2026JD047500 by Dtsch Zentrum F. Luft-U. Raum Fahrt In D. Helmholtz Gemein., Wiley Online Library on [11/11/2026]. See the Terms and Conditions (https://onlinelibrary.wiley.com/terms-and-conditions) on Wiley Online Library for rules of use; OA articles are governed by the applicable Creative Commons License

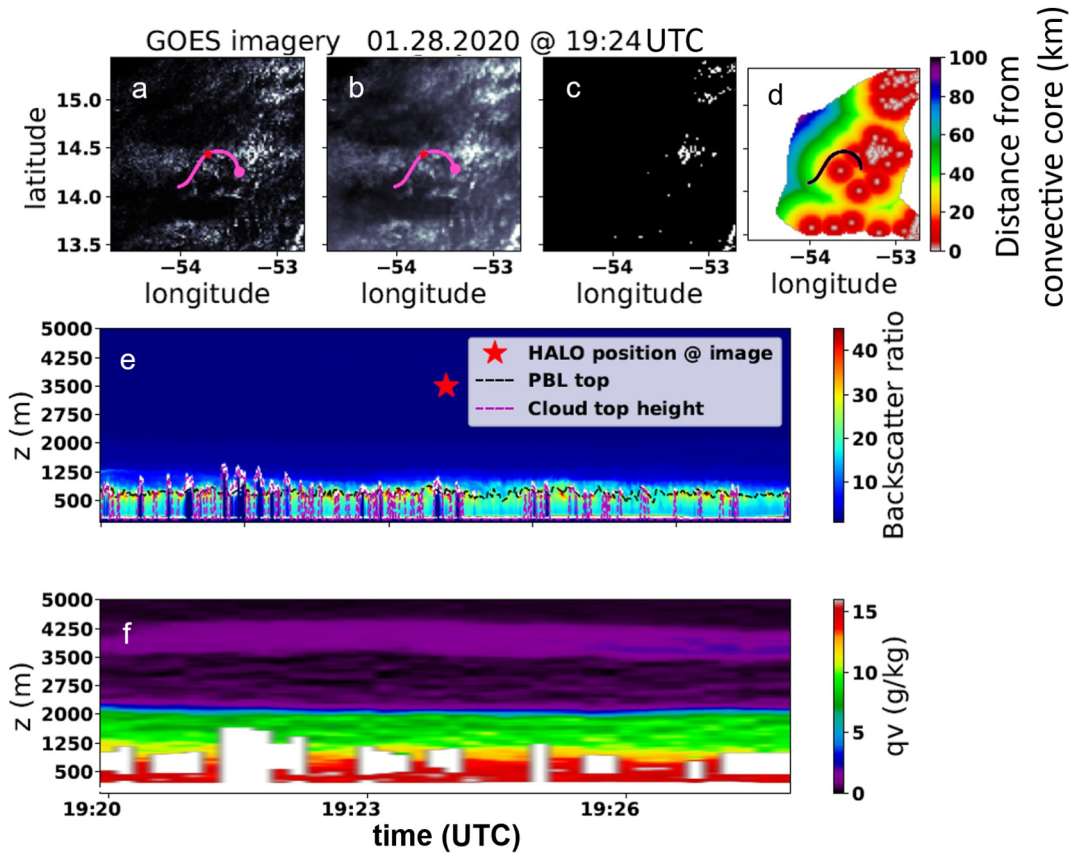

Figure 3. Same as Figure 2 but for the 28th of January at 19:24 UTC. A day dominated by shallower convection with smaller clouds.

mask, as the thresholds are taken from the distribution of cloud signals that depends on the sensitivity of the cloud mask. A more relaxed cloud mask that defines any suspicious pixel as a cloud increases the fraction of weak cloud signals in the distribution, pushing the dynamic thresholds (based on chosen percentiles) to lower values, thereby increasing the size of the convective cores (Figure S1 in Supporting Information S1). Roughly speaking, increasing cloud mask sensitivity is equivalent to reducing the percentiles used to define the dynamic thresholds of the cores. Larger cores decrease $\mathcal{D}_{\text{meso}}$; therefore, the scales presented in this study should be taken with caution, as they are subject to how one defines the convective cores. We will show, however, that $\mathcal{D}_{\text{meso}}$ is useful.

Sensitivity tests were conducted for the size of the domain ($2° \times 2°$ and $4° \times 4°$), percentiles used to define the cores (66, 75, and 90 percentiles), and cloud mask (GOES and the in-house developed cloud mask in Text S1 in Supporting Information S1). All tests yielded results that led to the same conclusions. The main difference is the scale of $\mathcal{D}_{\text{meso}}$, which affects the choice of the distance that should be selected for the far-field values.

3. Results

3.1. Gradients in Satellite Data on the Mesoscale

The CTZ is most commonly presented in the literature on the cloud scale using the distance from cloud metric ($\mathcal{D}_{\text{cld}}$). Figure 4 shows the mean solar radiance as a function of $\mathcal{D}_{\text{meso}}$, thereby presenting the solar CTZ at the mesoscale for the first time. The analysis includes only pixels that were not classified as clouds by the GOES cloud mask. The figure demonstrates that non-cloudy sky reflectance systematically increases toward convective cores across all analyzed days of the EUREC^{4}A field campaign, with their varying cloud patterns. The aerosol loading on each day can be interpreted by the mesoscale background reflectivity, indicated by a black dashed line (Figure 4). Information on cloud patterns is given in Table 1 and Figure 11. We note here that the mesoscale background signal represents the driest regions farthest away from the convective core, as opposed to the "pure"

21698996, 2026, 21, Downloaded from https://agupubs.onlinelibrary.wiley.com/doi/10.1029/2026JD047500 by Dtsch Zentrum F. Luft-U. Raum Fahrt In D. Helmholtz Gemein., Wiley Online Library on [11/11/2026]. See the Terms and Conditions (https://onlinelibrary.wiley.com/terms-and-conditions) on Wiley Online Library for rules of use; OA articles are governed by the applicable Creative Commons License

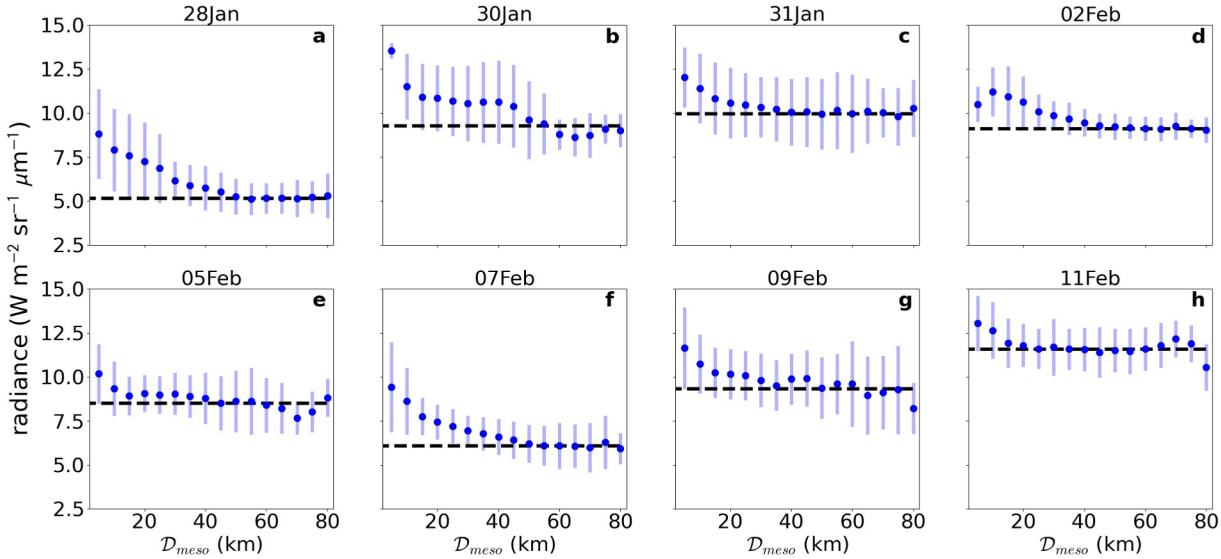

Figure 4. The increase of non-cloudy sky solar radiance on the mesoscale. Analysis of Geostationary Operational Environmental Satellite-Advanced Baseline Imager images at 0.86 μm. Each panel shows the mean and standard deviation of solar radiance versus distance from convective cores (D_{meso}) in 5 km bins for each analyzed day. The analysis includes only pixels that were not defined as clouds by the GOES cloud mask. The dashed horizontal line is the mesoscale background signal, calculated as the mean of all pixels with $D_{\text{meso}} > 50$ km.

clear-sky signal that is calculated at the cloud scale and represents pixels unaffected by cloud presence. The D_{meso} values used to define the far-field (mesoscale background) regions vary around 50 km, depending on the available values for each cloud field.

The increasing reflectance with decreasing D_{meso} in Figure 4 can be explained as follows: the convective cores are regions in which fluctuations in the environmental conditions favor cloud formation. Enhanced convective activity can reinforce itself by generating mesoscale circulations that promote moisture aggregation and deepen the boundary layer (Bretherton & Blossey, 2017; Janssens et al., 2023). Resulting gradients in column-integrated humidity can drive gradients in AOD and haze that directly increase clear-sky reflectivity. Cloud density is also expected to increase with humidity, increasing the reflectance of supposedly non-cloudy pixels through the presence of undetected clouds and three-dimensional radiative transfer effects.

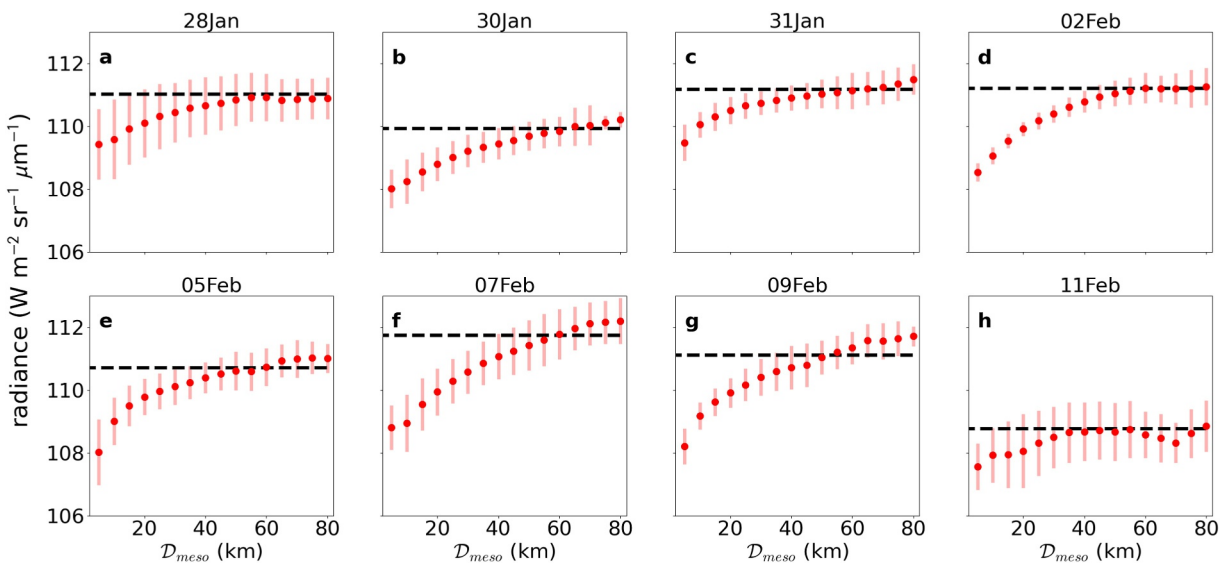

Figure 5. The decrease of non-cloudy sky thermal radiance on the mesoscale. Same as Figure 4 but for the thermal radiation using the 11.2 μm channel.

21698996, 2026, 21, Downloaded from https://agupubs.onlinelibrary.wiley.com/doi/10.1029/2026JD047500 by Dtsch Zentrum F. Luft-U. Raum Fahrt In D. Helmholtz Gemein., Wiley Online Library on [11/11/2026]. See the Terms and Conditions (https://onlinelibrary.wiley.com/terms-and-conditions) on Wiley Online Library for rules of use; OA articles are governed by the applicable Creative Commons License

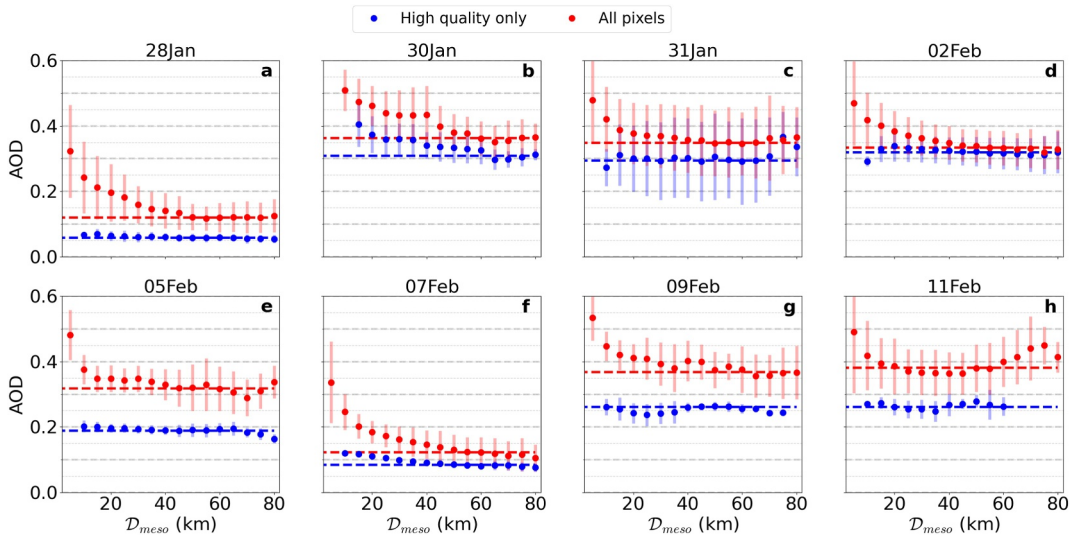

Figure 6. Aerosol optical depth (AOD) gradients on the mesoscale. Same as Figure 4 but for GOES AOD retrievals. Red is for all AOD-retrieved pixels while blue is for only the high-quality flagged pixels.

Applying the same analysis as in Figure 4, but using a more sensitive cloud mask, shows a large decrease in the deviation of reflectance from the mesoscale background values (not shown). This highlights a significant contribution of undetected clouds to the mesoscale CTZ signal observed when using the standard GOES cloud mask.

Figure 5 presents the same analysis for the longwave-infrared radiation. The decrease in signal near convective cores can be thought of as the "greenhouse" effect of moisture aggregation and undetected clouds. Such an effect was demonstrated at the cloud scale (Eytan et al., 2020), and was recently attributed to mesoscale processes (Rixen et al., 2025). While the mesoscale background values characterize the far-field humidity (e.g., 11 February corresponds to the day of deepest convection, with cloud tops reaching 5 km), the small $\mathcal{D}_{\text{meso}}$ bins capture information about CTH. This is illustrated by 28 January, a day dominated by shallow convection, which exhibits the highest radiance values at $\mathcal{D}_{\text{meso}} = 5$ km.

Figure 6 illustrates how GOES AOD retrievals respond to the identified mesoscale gradients. The figure is analogous to Figure 4 but shows AOD for two retrieval-quality categories: high-quality retrievals only (blue) and all retrieved pixels (red). The high-quality flag identifies pixels retrieved under optimal conditions, excluding cloud contamination and other challenging conditions known to degrade retrieval performance. For most days, the high-quality retrievals exhibit nearly constant AOD as a function of $\mathcal{D}_{\text{meso}}$, consistent with the common assumption that AOD is horizontally homogeneous at sub-mesoscale. However, this behavior contradicts the physical arguments presented in the paragraph above that consider mesoscale humidity gradients. Even clear-sky regions unaffected by cloud contamination would be expected to show AOD enhancement of 20%–80% simply due to aerosol humidification (Haslett et al., 2019; Hu et al., 2025). This discrepancy suggests that the retrievals fail to capture humidification signals on the mesoscale. We note that high-quality retrievals are preferentially located farther from clouds (see Figure 1).

In contrast, the red curve representing all retrieved pixels (dominated by low-quality retrievals) shows increased AOD that closely follows the enhanced reflectance signal in Figure 4. While this response is expected, the quantitative accuracy of these values is uncertain because these retrievals are prone to biases associated with undetected clouds and three-dimensional radiative transfer effects.

For the remainder of this manuscript, we use WALES LiDAR observations to obtain a more detailed view of the CTZ structure and its contributing components across the mesoscale.

21698996, 2026, 21, Downloaded from https://agupubs.onlinelibrary.wiley.com/doi/10.1029/2026JD047500 by Dtsch Zentrum F. Luft-U. Raum Fahrt In D. Helmholtz Gemein., Wiley Online Library on [11/11/2026]. See the Terms and Conditions (https://onlinelibrary.wiley.com/terms-and-conditions) on Wiley Online Library for rules of use; OA articles are governed by the applicable Creative Commons License

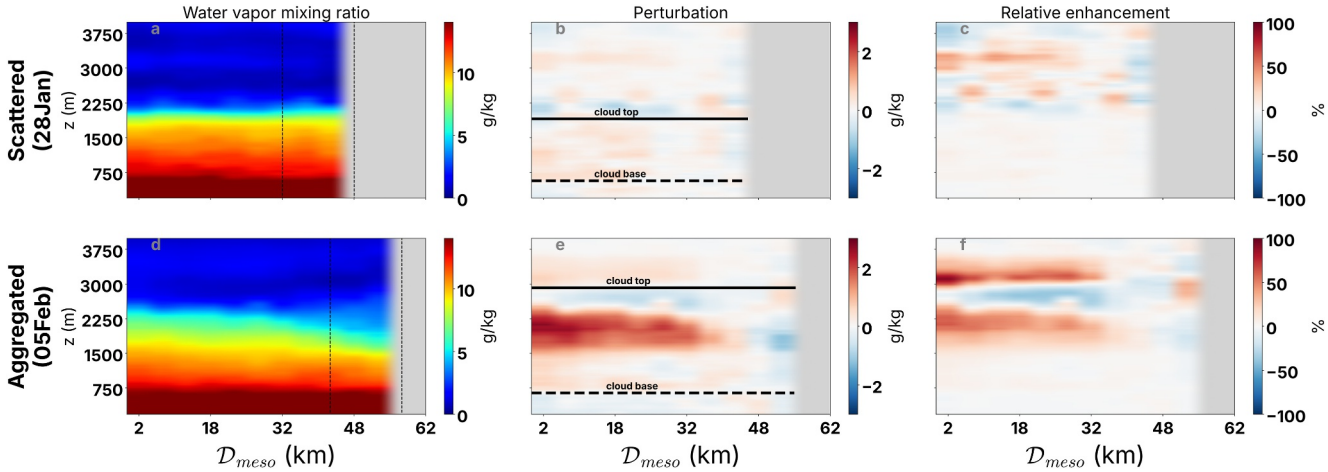

Figure 7. Humidity profiles of scattered versus aggregated convection. Mean profiles of specific humidity on the mesoscale obtained from the WALES retrievals (panels a, d) for 2 days: 28 Jan (representing scattered convection), and 05 Feb, which had large aggregated cloud structures. All samples are for cloud-free columns. The far field (farthest 20 km), marked by dashed lines, is averaged to give the mesoscale background value, which is then subtracted from the mean profiles to get the perturbation (b), (e) and relative enhancement (c), (f) profiles. The relative enhancement is calculated as $\frac{q_v(\mathcal{D}_{\text{meso}},z)-\overline{q_v(z)}}{\overline{q_v(z)}}$, where q_v is specific humidity and $\overline{q_v(z)}$ is the background profile. The levels of cloud base and top were defined by WALES daily mean cloud-top height retrievals (1st and 99th percentiles, respectively), and are marked by black horizontal lines in panels (b, e).

3.2. Humidity, Aerosol, and Cloud Structures for Aggregated Versus Scattered Convection

In this section, we compare the structure of the CTZ between aggregated and scattered convection using two representative days of the EUREC^{4}A field campaign. The 28 January day was dominated by shallow convection (see Figure 3) while the 05 February day (Figure 2) had large aggregated Flowers cloud structures (Table 1). The CTZ structure is analyzed in $\mathcal{D}_{\text{meso}}$–$z$ space by averaging WALES profiles within bins of $\mathcal{D}_{\text{meso}}$ derived from GOES imagery. Throughout this study, $\mathcal{D}_{\text{meso}}$ bins are 5 km wide.

Figures 7–9 present the structure of non-cloudy columns (as identified by the WALES cloud mask) for humidity and aerosol scattering properties (i.e., aerosol backscatter ratio, β_r; and extinction, α_{aer}). While β_r is a more robust and straightforward proxy of aerosol scattering at high-resolution, α_{aer} complements with more interpretable physical units that, after vertical integration, can be compared to satellite observations.

Figures 7a and 7d show the mean water vapor mixing ratio (q_v) profiles as a function of $\mathcal{D}_{\text{meso}}$ for 28 January and 05 February, respectively. The humidity perturbation (panels b,e) is defined as the difference between the profile

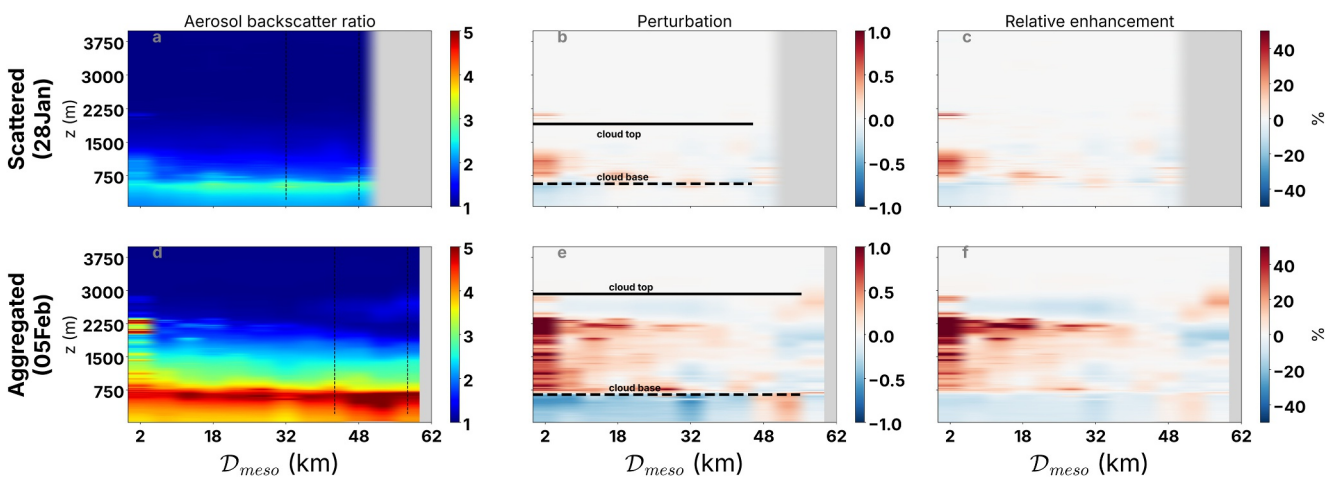

Figure 8. Aerosol backscatter ratio profiles of scattered versus aggregated convection. Same as Figure 7 but for the aerosol backscatter ratio.

21698996, 2026, 21, Downloaded from https://agupubs.onlinelibrary.wiley.com/doi/10.1029/2026JD047500 by Dtsch Zentrum F. Luft-U. Raum Fahrt In D. Helmholtz Gemein., Wiley Online Library on [11/11/2026]. See the Terms and Conditions (https://onlinelibrary.wiley.com/terms-and-conditions) on Wiley Online Library for rules of use; OA articles are governed by the applicable Creative Commons License

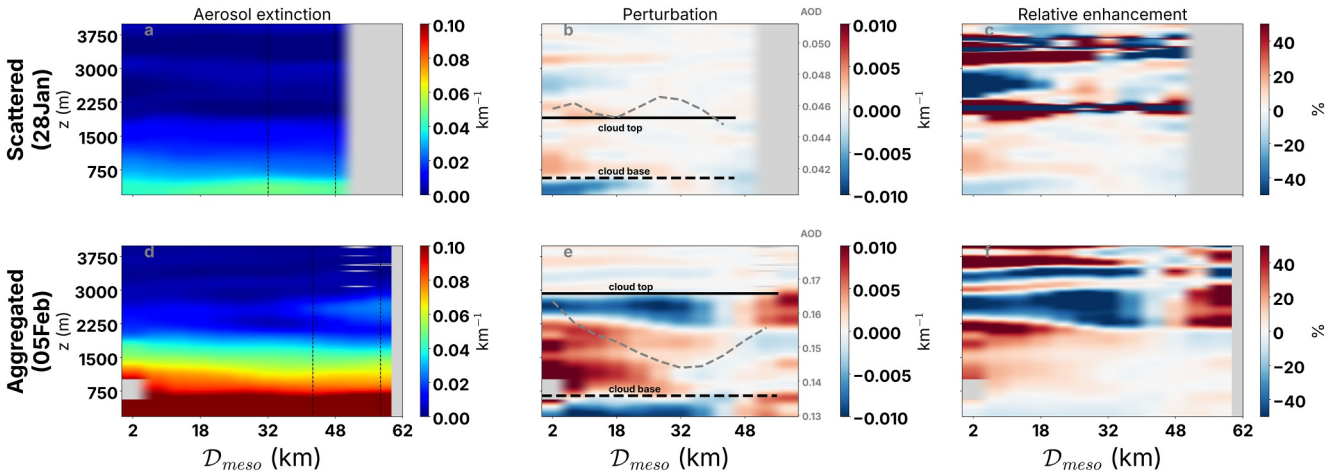

Figure 9. Aerosol extinction profiles of scattered versus aggregated convection. Similar to Figure 8 but for the aerosol extinction. The z-$\mathcal{D}_{\text{meso}}$ space is smoothed with a Gaussian filter with width of 105 m in the vertical and 5 km in the horizontal. Gray dashed curves in panels b, e show aerosol optical depth, which was calculated by vertical integration of the extinction up to the aircraft flight altitude of ∼10 km. During the integration, missing values (NaNs) were filled using the mesoscale background profile.

in each $\mathcal{D}_{\text{meso}}$ bin and the mesoscale background profile, while the relative enhancement (panels c,f) is the perturbation normalized by the mesoscale background profile. For the rest of the manuscript, mesoscale background values are defined by averaging the far-field region ($40 < \mathcal{D}_{\text{meso}} < 60$ km), consistent with the 50 km value in Figure 4. The only exception is the 28 January case, for which contamination by clouds with high cloud-top-height (CTH) is evident (shown and discussed below).

Cloud fields dominated by small, scattered clouds do not exhibit a strong humidity anomaly pattern (Figure 7b). In contrast, aggregated convection composed of Flowers clouds exhibits a distinct positive humidity anomaly centered near 2 km altitude (Figure 7e). This humidified layer is consistent with detrainment from the large aggregated clouds that reach the trade-wind inversion. Such layers were described in the past using an S-band, dual-polarization Doppler radar (Davison, Rauber, & Di Girolamo, 2013; Davison, Rauber, Di Girolamo, & LeMone, 2013). The relative enhancement field (Figure 7f) shows that these anomalies can reach as high as 50%. The signal of humidity injection into the free troposphere, as demonstrated in Figure 2f appears as a pattern of positive anomalies above cloud top at low $\mathcal{D}_{\text{meso}}$.

Figure 8 compares the aerosol radiative properties of the two case studies using β_r. The 28 January case represents a relatively pristine environment, characterized by weak mean aerosol β_r, whereas the 05 February case exhibits enhanced aerosol loading associated with a dust plume mixed into the boundary layer (see Table 1). A notable feature in Figure 8e, and to some extent also in Figure 8b, is a reduction in β_r below cloud base and in the vicinity of the convective cores. This pattern is suggestive of precipitation and cold-pool processes that promote aerosol scavenging, although ancillary observations and dedicated modeling studies would be required to confirm this interpretation.

The analysis in this manuscript primarily relies on the 532 nm HSRL channel of WALES, which provides higher retrieval accuracy. However, longer wavelengths in the solar spectrum can be advantageous for analyzing the CTZ, as their greater sensitivity to larger particles enhances the contrast between near-cloud regions and the background signal (Eytan et al., 2025; Várnai & Marshak, 2018). Analysis similar to Figure 8 is presented in the Supporting Information S1 for the 1,064 nm channel of WALES, which is not an HSRL channel (Text S5 in Supporting Information S1).

The β_r perturbation on 28 January (Figure 8b) illustrates the vertical redistribution of aerosol by shallow, small clouds over a limited spatial extent, bounded by their vertical development up to ∼1.2 km (see Figure 3e). This positive aerosol-scattering perturbation corresponds to a relative enhancement of about 50% in the cloud layer. For the aggregated convection case, a pronounced detrainment layer is evident (Figure 8e), consistent with the associated humidity structure (Figure 7e). The relative enhancement of this structure reaches 200% in a thin layer. The magnitude of this signal, occurring in the boundary layer that contributes the most to total AOD (Bourgeois

21698996, 2026, 21, Downloaded from https://agupubs.onlinelibrary.wiley.com/doi/10.1029/2026JD047500 by Dtsch Zentrum F. Luft-U. Raum Fahrt In D. Helmholtz Gemein., Wiley Online Library on [11/11/2026]. See the Terms and Conditions (https://onlinelibrary.wiley.com/terms-and-conditions) on Wiley Online Library for rules of use; OA articles are governed by the applicable Creative Commons License

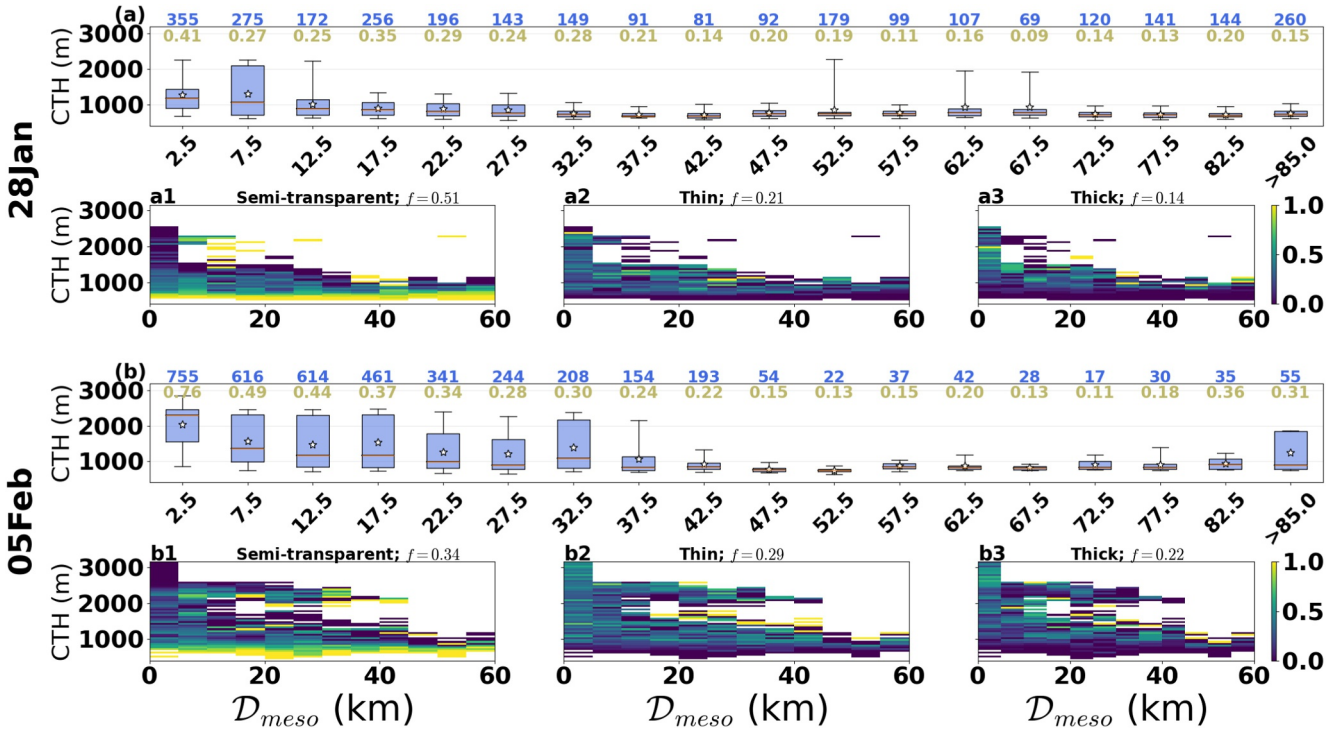

Figure 10. Cloud distribution for scattered versus aggregated convection. Cloud-top height (CTH) and optical thickness for the cloudy columns along the distance from convective cores ($\mathcal{D}_{\text{meso}}$). (a) CTH distributions for the 28 Jan day in each distance bin. Each boxplot shows the median (red line), mean (star), 25th and 75th percentiles (blue box), and 1st and 99th percentiles (error bars). Number of cloud samples in each bin is given in blue digits above the boxplots, while the fraction of cloudy samples in the bin is given in golden digits. The cloudy columns are also categorized into: semi-transparent clouds with cloud optical thickness ($\tau_{\text{cld}} < 0.5$), Thin ($1 < \tau_{\text{cld}} < 3$), and Thick ($\tau_{\text{cld}} > 3.5$). The fraction of each category in each CTH-$\mathcal{D}_{\text{meso}}$ bin is given in panels a1-3 and the fraction of all cloud samples (f) is given next to the category's subtitle. Panels b and the following b1-3 are the same but for the 05 Feb day.

et al., 2018), suggests that it can account for a significant fraction of the ~10% enhanced reflectance observed in Figure 4.

Figure 9 shows the extinction field for the same cases. The $z - \mathcal{D}_{\text{meso}}$ field of α_{aer} was noisy (see Section 2.1), and therefore smoothed using a Gaussian filter (the non-smoothed field is provided in the Text S2 in Supporting Information S1). The overall picture remains consistent despite the smoothing, which blurs fine-scale coherent structures such as the thin detrainment layer evident in β_r (Figure 8). The dashed gray curves overlaid on the perturbation panels show the mean LiDAR-derived AOD as a function of $\mathcal{D}_{\text{meso}}$, computed by vertical integration of α_{aer}. This AOD profile can be compared with the satellite-based retrievals in Figure 6, noting that it is limited to the aircraft altitude, whereas the satellite retrieval represents the full atmospheric column. Nevertheless, as noted above, most of the AOD originates within the first few kilometers above the surface, well below the aircraft flight level.

For the 28 January case, the LiDAR-derived AOD (gray curve in Figure 9b) shows agreement with the GOES high-quality retrieval, in both the shape and magnitude of the $\mathcal{D}_{\text{meso}}$ dependence (blue curve in Figure 6a). The 05 February case highlights the complementary strengths and limitations of the two observing platforms. The LiDAR retrievals are more direct observations with higher sensitivity and fewer assumptions, but are limited by the smaller number of available profiles. Within the first ~40 km from the convective cores, the LiDAR AOD decreases with increasing $\mathcal{D}_{\text{meso}}$, consistent with both the theoretical expectation and the perturbation field shown in Figure 9d. However, the LiDAR AOD in the far-field is clearly affected by contamination of high-α_{aer} values that inflate the mesoscale background profile estimate, causing the curve to increase again when $\mathcal{D}_{\text{meso}} > 40$ km. Such noise is suppressed in the satellite retrievals (Figure 6e), which average over all pixels within the image domain. Despite the ambiguity, the mesoscale background LiDAR AOD can be estimated at approximately 0.15, lower than the GOES retrieval, which is approximately constant at 0.2.

21698996, 2026, 21, Downloaded from https://agupubs.onlinelibrary.wiley.com/doi/10.1029/2026JD047500 by Dtsch Zentrum F. Luft-U. Raum Fahrt In D. Helmholtz Gemein., Wiley Online Library on [11/11/2026]. See the Terms and Conditions (https://onlinelibrary.wiley.com/terms-and-conditions) on Wiley Online Library for rules of use; OA articles are governed by the applicable Creative Commons License

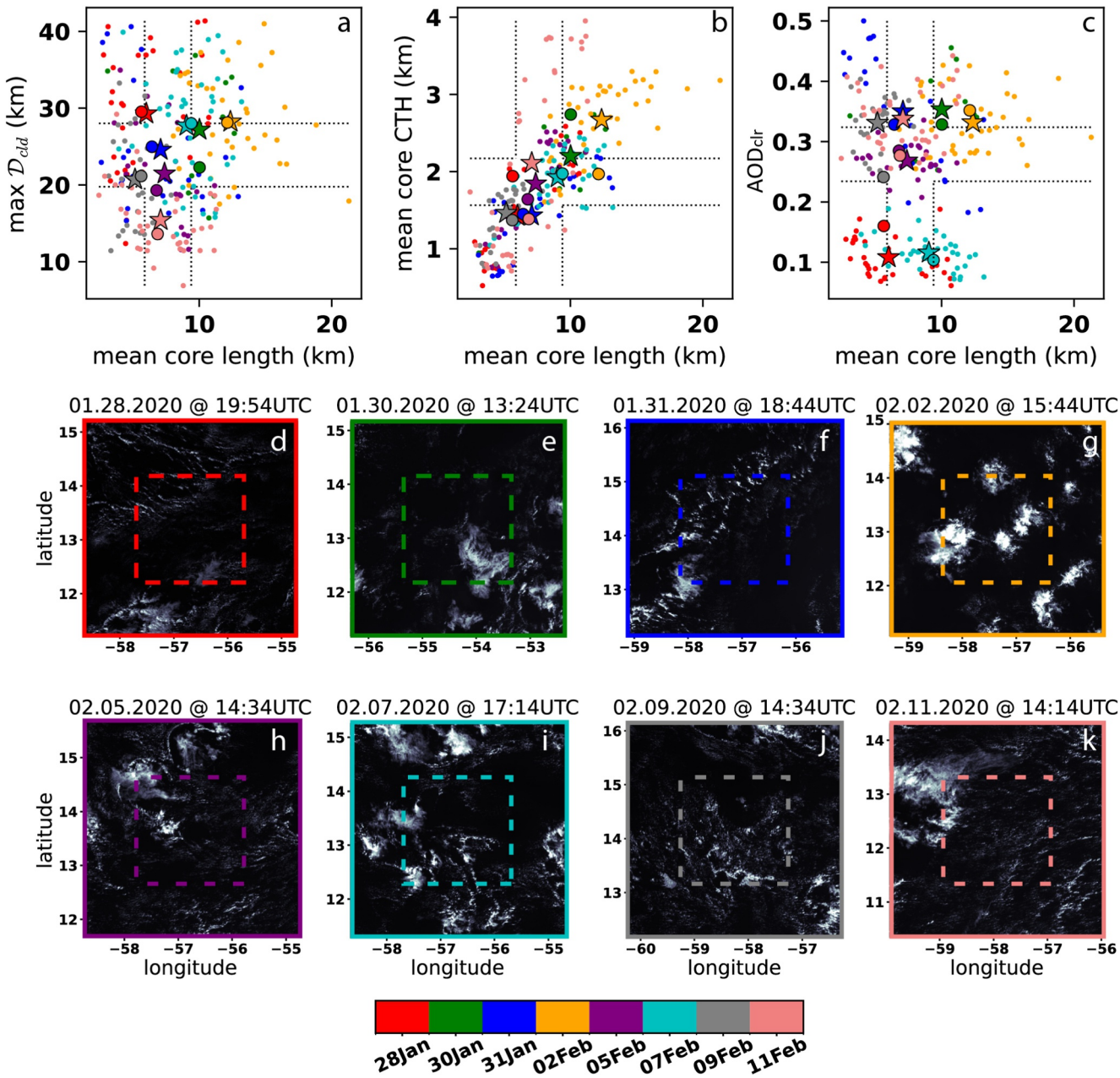

Figure 11. Cloud field patterns and properties on 2D spaces. Scatter plots of mean convective core length $\left(\tilde{L}_{\text{core}}\right)$ versus: (a) maximum distance from cloud ($D_{\text{cld}}^{\text{max}}$), (b) mean convective core cloud-top height, and (c) pure clear-sky aerosol optical depth (AOD) (AOD_{clr}) obtained from GOES AOD retrievals where $\mathcal{D}_{\text{cld}} > 15$ km. Dashed lines indicate terciles of each metric. Colors denote different analyzed days, and stars mark the daily mean in each two-dimensional space. Large dots identify the image that best represents the mean cloud pattern of each day. These representative images were selected as those with the smallest Euclidean distance to the daily mean in the $\tilde{L}_{\text{cld}}$–$D_{\text{cld}}^{\text{max}}$ space (panel a) and are shown in panels (d–k). Each panel presents a 4° × 4° domain to provide a broader spatial context for the cloud pattern on that day. The representative images are confined by a dashed line in the center. All images use the same color scale, ranging from 0 to 200 W m^{-2} sr^{-1} μm^{-1}, black to white, respectively.

Next, we turn to analyzing the cloud structure on the mesoscale using WALES, which is sensitive to small and optically thin clouds that are abundant in these regions (Leahy et al., 2012; Mieslinger et al., 2022) and are often undetected by passive imagers like GOES (Jiménez, 2020). Clouds that are not detected by satellite imagers contribute significantly to low-confidence AOD retrievals (Schwarz et al., 2017), and there are multiple lines of evidence suggesting that undetected clouds play an important role in the CTZ radiative signature (Eytan et al., 2025).

21698996, 2026, 21, Downloaded from https://agupubs.onlinelibrary.wiley.com/doi/10.1029/2026JD047500 by Dtsch Zentrum F. Luft-U. Raum Fahrt In D. Helmholtz Gemein., Wiley Online Library on [11/11/2026]. See the Terms and Conditions (https://onlinelibrary.wiley.com/terms-and-conditions) on Wiley Online Library for rules of use; OA articles are governed by the applicable Creative Commons License

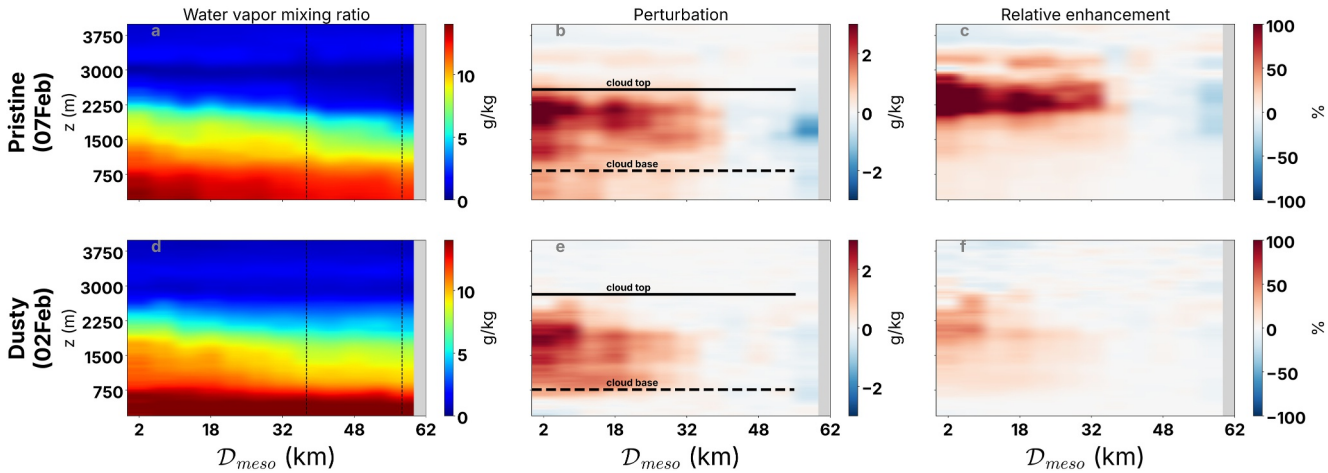

Figure 12. Humidity profiles of pristine versus dusty days for aggregated cloud fields. Same as Figure 7 but for the days 02 Feb (dusty) and 07 Feb (pristine).

The distribution of CTH in $\mathcal{D}_{\text{meso}}$ bins for 28 January is presented using boxplots in Figure 10a. This plot shows that 28 January was dominated by shallow clouds with a largely homogeneous distribution along $\mathcal{D}_{\text{meso}}$. The occasional presence of deeper clouds in some of the images elongates the CTH distribution toward higher altitudes near the convective cores. A signature of such deeper clouds when located just outside the analyzed domain is apparent at $\mathcal{D}_{\text{meso}} \sim 50$ km. For this reason, the far field is defined as $30 < \mathcal{D}_{\text{meso}} < 50$ km in Figures 7 and 8, panels a–c.

To further characterize the mesoscale cloud structure, the cloud samples are binned in CTH–$\mathcal{D}_{\text{meso}}$ space and separated into three categories according to their cloud optical thickness (τ_{cld}):

1. *Semi-transparent clouds* with $\tau_{\text{cld}} < 0.5$
2. *Thin clouds* with $1 < \tau_{\text{cld}} < 3$
3. *Thick clouds* with $\tau_{\text{cld}} > 3.5$

The semi-transparent clouds are defined according to the known limitations of multi-spectral satellite imagers (e.g., MODIS and GOES) in detecting clouds with such low τ_{cld} (Ackerman et al., 2008; NOAA GOES-R Algorithm Working Group & & GOES-R Program Office, 2018). Thin clouds are commonly defined in the literature as clouds with $\tau_{\text{cld}} < 3$ (McCoy et al., 2023; Mieslinger et al., 2022; Wood, Tseng, et al., 2018). Note that the WALES retrieval loses sensitivity for $\tau_{\text{cld}} > 3$ because extinction prevents the LiDAR from penetrating deeper into the clouds.

The frequency of occurrence (f) of each cloud category is reported next to the subtitle of Figure 10a1–3. These frequencies show that 28 January was dominated by shallow optically thin, and semi-transparent clouds that account for 21 and 51% of the cloud samples, respectively. The fraction of each category in each CTH–$\mathcal{D}_{\text{meso}}$ bin is plotted in Figure 10a1–3, illustrating that optically thin clouds with CTH below 1 km dominate the cloud distribution as seen by the WALES LiDAR. These clouds reside near cloud base and are confined by the trade wind convective inhibition layer (Albright et al., 2023). These results suggest that such hazy, weak, cloudy features, which are largely undetected by spaceborne observations, constitute a significant component of the CTZ in regimes of scattered shallow convection.

Figure 10b and its sub-panels present the same analysis for 05 February. While cloud properties are similar to 28 January far from the convective cores, the CTH distribution extends up to the cloud-layer top at approximately 2 km closer to the cores. This is consistent with the detrainment layer shown in Figures 7 and 8 that extends out to $\mathcal{D}_{\text{meso}} \sim 35$ km, suggesting that this layer contains cloud droplets. Figure 10b1,2 support this interpretation by showing that this layer is dominated by optically thin clouds.

Overall, these results indicate that the mesoscale structure and composition of the CTZ depend on cloud morphology. Aggregated cloud fields consist of a range of optically thin cloud types that reside in an environment with enhanced humidity that increases aerosol size; both are key components of the CTZ. Moreover, aggregation

21698996, 2026, 21, Downloaded from https://agupubs.onlinelibrary.wiley.com/doi/10.1029/2026JD047500 by Dtsch Zentrum F. Luft-U. Raum Fahrt In D. Helmholtz Gemein., Wiley Online Library on [11/11/2026]. See the Terms and Conditions (https://onlinelibrary.wiley.com/terms-and-conditions) on Wiley Online Library for rules of use; OA articles are governed by the applicable Creative Commons License

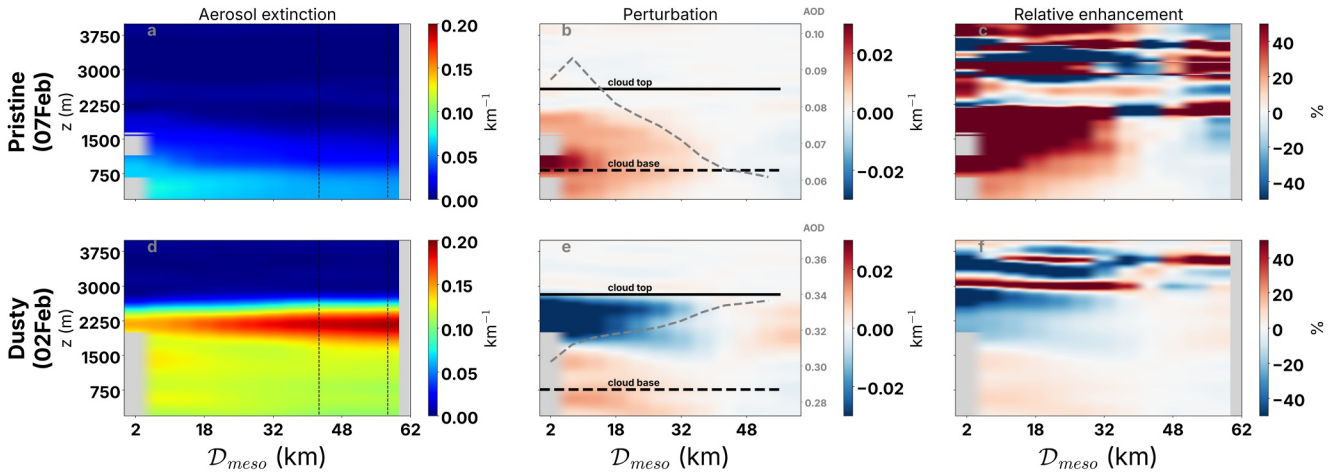

Figure 13. Aerosol extinction profiles of pristine versus dusty days of aggregated clouds. Same as Figure 9 but for 02 Feb (dusty) and 07 Feb (pristine). The white band near the cores in panels (a–c) represents bins with less than 30 samples due to high cloud density in those regions that do not permit extinction retrievals.

of moisture and clouds into large humid patches leaves extensive cloud-free voids far from them, where drier air and the absence of optically thick clouds weaken the CTZ signature.

3.3. The Effect of Dust on the Aerosol–Cloud Transition Zone

Following the results of the section above, we extend the case study analysis to other days of the EUREC^{4}A field campaign. Figure 11 shows scatter plots of different properties of the cloud fields for all analyzed GOES images and all analyzed days. Figure 11a shows the mean convective core length ($\bar{L}_{\text{core}}$), calculated as the square root of the mean convective core area versus the maximum distance from cloud ($\mathcal{D}_{\text{cld}}^{\max}$; defined by the GOES-ABI cloud mask), which represents the largest cloud-free void in the cloud field. Janssens et al. (2021) showed that similar metrics (i.e., typical cloud length and largest cloud-free void) are almost orthogonal and explain ∼30% of the variance of 21 commonly used metrics for quantifying cloud-field organization. We use the typical convective core size rather than the typical cloud size due to the coarse resolution of GOES that tends to miss small clouds.

The 2D space in Figure 11a can be used to classify the different cloud field patterns and infer the dominant cloud patterns for each day. As an example, the top-right corner of the 2D space represents aggregated Flowers clouds, while the bottom-left corner represents scattered convection in which small clouds are spread over the entire domain. A caveat of this approach is that Flowers clouds are often surrounded by small cumuli that reduce $\mathcal{D}_{\text{cld}}^{\max}$. In such cases, a metric that quantifies CTH provides additional information; therefore, Figure 11b plots $\bar{L}_{\text{core}}$ against the mean convective-core top. Figure 11c shows $\bar{L}_{\text{core}}$ versus AOD_{clr}, which represents the background (pure clear-sky) AOD of each cloud field (i.e., image) and is calculated as the mean of all pixels with $\mathcal{D}_{\text{cld}} > 15$ km.

To show the typical cloud patterns on each day and how these patterns manifest in the two-dimensional parameter spaces, Figures 11d and 11k shows the images that are most representative of each analyzed day. This representative image is defined as the image with the smallest Euclidean distance to the daily mean in the $\bar{L}_{\text{cld}}$–$\mathcal{D}_{\text{cld}}^{\max}$ space (Figure 11a), indicated by a large dot in each panel of Figures 11a–11c. The daily mean is marked with a star. Figure 11, which provides quantitative metrics of key properties of the cloud fields and their patterns, visualizes the cloud patterns of the different analyzed days, and the variability among the days and during each day.

Figures 11a and 11b show the similarities between 02 February and 07 February, both being days with large aggregated Flowers clouds. Figure 11c, on the other hand, shows an important difference between these days; while 02 February shows high AOD_{clr} values due to a thick dust layer near cloud tops (Gutleben et al., 2022; Narenpitak et al., 2021), the clouds on 07 February experienced pristine conditions, as the dust had already been washed out. Analyzing these 2 days allows us to study the effect of background aerosol profiles on the CTZ.

21698996, 2026, 21, Downloaded from https://agupubs.onlinelibrary.wiley.com/doi/10.1029/2026JD047500 by Dtsch Zentrum F. Luft-U. Raum Fahrt In D. Helmholtz Gemein., Wiley Online Library on [11/11/2026]. See the Terms and Conditions (https://onlinelibrary.wiley.com/terms-and-conditions) on Wiley Online Library for rules of use; OA articles are governed by the applicable Creative Commons License

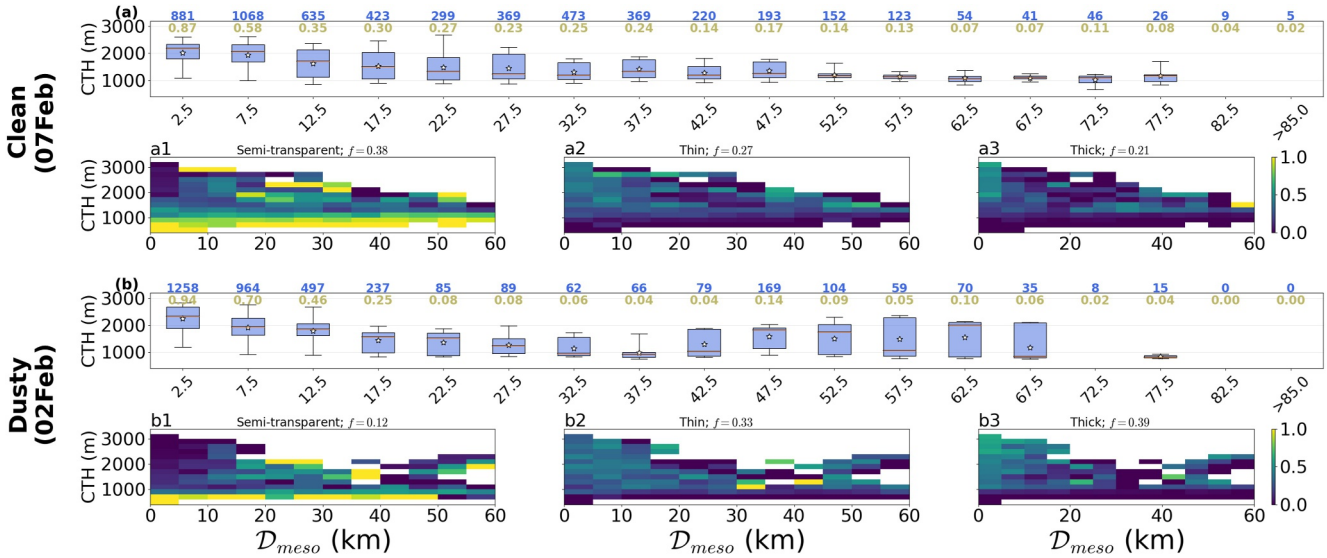

Figure 14. Cloud distribution for pristine versus dusty days. Same as Figure 10 but for the days 02 Feb (dusty) and 07 Feb.

Figures 12 and 13 are the same as Figures 7 and 9, respectively, except that they compare the humidity and extinction fields for dusty versus non-dusty aggregated Flowers cloud fields. The dust layer is apparent at an altitude of 2.2 km (Figure 13d).

At first glance, the humidity patterns in Figures 12a and 12d look quite similar due to similar cloud-field dynamics driven by moisture aggregation, but a more detailed look shows a couple of small differences. Far from the convective cores, 02 February is shown to have a thin low-humidity layer above 2,230 m, whereas 07 February has no such layer (see the colors of Figures 12a and 12d). This is probably due to moisture transport that accompanies the dusty air transported to the Atlantic (Gutleben et al., 2020, 2022). The effect of this on the CTZ structure is more pronounced in the relative enhancement fields (Figures 12c and 12f), where 02 February does not show enhancement below cloud top (i.e., the detrainment layer), probably due to the higher background values in the far field. 07 February shows the familiar detrainment layers (Figure 12c) that are also observed for 05 February.

Comparing the 3 days of aggregated convection that included Flowers clouds provides insights into the key role of the background aerosol profile in shaping the mesoscale CTZ structure. The three different days can roughly be categorized as pristine (07 February), aerosol-laden boundary layer (05 February), and dusty (02 February) (see Figures 9e, 11c, 13b, and 13e). In situ measurements of aerosol concentration at cloud base made on the French SAFIRE ATR42 research aircraft with the Ultra-High Sensitivity Aerosol Spectrometer (UHSAS) (Coutris and Ehses (2021); Bony et al. (2022)) support this categorization. The UHSAS, measuring dry aerosol in the range of 0.06–1 microns, showed mean values around 80, 350, and 400 cm^{-3} for the 07 February, 05 February, and 02 February, respectively (not shown).

The detrained layer on 02 February is shown (Figure 13e) as a negative analogue to 05 February, where the pattern of the layer appears as a negative perturbation. The coarse resolution of the extinction retrieval somewhat smooths the negative pattern in Figure 13. However, the z-$\mathcal{D}_{\text{meso}}$ space of β_r of both 532 and 1,064 nm channels shows a much more coherent structure of the negative detrainment layer (Figures S4e and S6e in Supporting Information S1). It seems that in the case of 02 February, the convective cores transport cleaner air from the sub-cloud layer and process it by precipitation scavenging, making it clearer relative to the high background value of the dust layer. The clearing of the upper boundary layer drives a reduction in AOD near the convective cores (Figure 13e), highlighting the advantage of LiDAR observations in resolving vertical structure. From a satellite perspective alone, this AOD decrease might have been attributed to cold-pool processes cleaning the mixed layer below cloud base; however, the LiDAR observations indicate that it is primarily associated with dust-free air detrained from the top of the cloud layer.

21698996, 2026, 21, Downloaded from https://agupubs.onlinelibrary.wiley.com/doi/10.1029/2026JD047500 by Dtsch Zentrum F. Luft-U. Raum Fahrt In D. Helmholtz Gemein., Wiley Online Library on [11/11/2026]. See the Terms and Conditions (https://onlinelibrary.wiley.com/terms-and-conditions) on Wiley Online Library for rules of use; OA articles are governed by the applicable Creative Commons License

21698996, 2026, 21, Downloaded from https://agupubs.onlinelibrary.wiley.com/doi/10.1029/2026JD047500 by Dtsch Zentrum F. Luft-U. Raum Fahrt In D. Helmholtz Gemein., Wiley Online Library on [11/11/2026]. See the Terms and Conditions (https://onlinelibrary.wiley.com/terms-and-conditions) on Wiley Online Library for rules of use; OA articles are governed by the applicable Creative Commons License

Some insights into the interactions of dust, humidity, and cloud processing can also be gained by analyzing the particle depolarization ratio (δ_{aer}) of the 532 nm channel. Spherical particles preserve light polarization and pure dust particles depolarize light (Groß et al., 2011, 2013; Haarig et al., 2018; Schotland et al., 1971), hence, one can use δ_{aer} to analyze changes in aerosol type in the z-$\mathcal{D}_{meso}$ space. Figures similar to 13 but for δ_{aer} are presented in Figure S5 in Supporting Information S1 to show how cloud processing and boundary layer mixing decrease δ_{aer} in the cloud layer near the cores at $\mathcal{D}_{meso} < 25$ km.

Figure 14 shows the cloud structures for 02 February and 07 February. The 07 February case exhibits many similarities to 05 February, including a comparable partitioning among cloud optical thickness classes and a similar dependence of the CTH distributions on $\mathcal{D}_{meso}$, although the detrainment layer is less pronounced and occurs on a smaller spatial scale.

In contrast, the 02 February case displays a distinctly different behavior. First, a pronounced peak of high CTH contamination is evident far from the cores at $\mathcal{D}_{meso} \sim 55$ km. Second, the partitioning among cloud optical thickness classes differs substantially, with semi-transparent clouds accounting for only 12% of the cloudy columns; a reduction that appears to result from fewer weak clouds in both the detrainment layers and near cloud base. It remains unclear whether this reflects reduced sensitivity of the WALES cloud mask under dusty conditions or a genuine physical response. This was tested and is not a consequence of the thick cloud contamination discussed above, and we believe that this is not an issue with the WALES cloud mask algorithm. We suggest two mechanisms by which the amount of semi-transparent clouds could be reduced:

1. Radiative–microphysical effects, whereby light absorption heats the particles, suppressing nucleation and condensation rates (Conant et al., 2002; Graßl, 1975).
2. Radiative–thermodynamic effects, whereby absorption by dust and biomass-burning aerosol, accompanied by elevated humidity, enhances radiative heating of the dust layer, increases atmospheric stability, and reduces cloud cover (Feingold et al., 2005; Gutleben et al., 2019; Koren et al., 2004).

Since optically thin clouds probably play a major role in the CTZ, and have a strong radiative effect that is challenging to estimate, the reduction of semi-transparent clouds under dusty conditions seems to be an interesting research question that cannot be resolved in this study with its limited number of observations.

4. Summary and Conclusions

More than half of the clear-sky area over the oceans is covered by the aerosol–cloud transition zone (CTZ), an ill-defined region that does not follow the classical definitions of either aerosols or clouds (Bar-Or et al., 2011; Eytan et al., 2020; Várnai & Marshak, 2009) and introduces biases to remote sensing retrievals of aerosol and humidity (John et al., 2011; Marshak et al., 2021). A separate line of research has focused on moisture aggregation and the organization of shallow convective clouds, which have received increasing attention for their roles in Earth's energy budget and cloud–climate feedbacks (Bretherton & Blossey, 2017; Janssens et al., 2023; Narenpitak et al., 2021).

In this study, we combine the two research fields to better understand the mesoscale structure of the CTZ and aerosol spatial distribution (Anderson et al., 2003). We suggest that moisture aggregation directly influences the spatial distribution of aerosol extinction through hygroscopic growth in humid environments. It also indirectly affects aerosols by modulating cloud organization and, consequently, the spatial structure of the CTZ. Moreover, the counterpart of moisture aggregation is the development of extensive dry cloud-free regions (Bretherton & Blossey, 2017) that should weaken the CTZ radiative effect.

Analysis of airborne WALES LiDAR measurements during the EUREC^{4}A field campaign, complemented by GOES-ABI observations, provides a new perspective on the horizontal and vertical organization of the CTZ and demonstrates that the CTZ has a mesoscale structure associated with the organization of shallow convection. Extending the conventional view of the CTZ as primarily a cloud-edge phenomenon, we characterize the mesoscale structure by introducing the distance from convective cores, $\mathcal{D}_{meso}$, as a complementary metric to the commonly used distance from the nearest cloud, $\mathcal{D}_{cld}$. While $\mathcal{D}_{cld}$ describes the local environment of individual clouds, $\mathcal{D}_{meso}$ captures gradients across cloud fields, from convective cores toward the drier regions at their periphery.

21698996, 2026, 21, Downloaded from https://agupubs.onlinelibrary.wiley.com/doi/10.1029/2026JD047500 by Dtsch Zentrum F. Luft-U. Raum Fahrt In D. Helmholtz Gemein., Wiley Online Library on [11/11/2026]. See the Terms and Conditions (https://onlinelibrary.wiley.com/terms-and-conditions) on Wiley Online Library for rules of use; OA articles are governed by the applicable Creative Commons License

The observations show that small cumulus cloud fields produce relatively weak mesoscale humidity gradients and perturbations in aerosol extinction. In contrast, aggregated convection produces extensive detrained layers of enhanced humidity and modified aerosol properties that can extend tens of kilometers from the convective cores. These detrained layers do not necessarily arise solely from the direct outflow of humidified particles from convective cores. They may also form through condensational growth of particles within the detrained humid layer near the trade-wind inversion, supported, for example, by gravity waves. Precipitation remnants could be another mechanism that contributes to the formation of such layers (Wood, Kuan-Ting et al., 2018).

The relationship between humidity and aerosol extinction is not always straightforward: precipitation scavenging, cold-pool dynamics, and cloud processing can reduce aerosol extinction near the humid convective cores. The manifestation of these processes depends on the background aerosol profile. Specifically, the dusty cases demonstrate that convective detrainment can appear as a negative perturbation in aerosol extinction relative to the background aerosol layer. These results illustrate that mesoscale aerosol variability reflects the combined effects of thermodynamic variability, detrainment, precipitation, and the background aerosol environment. The sensitive vertically resolved LiDAR observations further reveal that a substantial fraction of the cloudy atmosphere in the CTZ consists of optically thin clouds that are not detected by passive satellite imagers such as GOES-ABI. These include shallow forced clouds near cloud base as well as thin clouds associated with detrained layers near the trade-wind inversion.

This study shows that the mesoscale behavior of retrieved AOD depends strongly on retrieval quality: when all retrievals are considered (including unreliable data), AOD increases toward the convective cores as physically anticipated, whereas high-quality retrievals alone do not show the expected mesoscale trend. Thus, cloud screening intended to reduce retrieval biases may simultaneously remove portions of the atmosphere in which physically meaningful aerosol variability occurs. Avoiding AOD retrievals near clouds causes a sampling bias in global observations of AOD that biases estimates of aerosol budgets and radiative effects. All of the above suggest that improving our understanding of the mesoscale patterns of the CTZ will improve our understanding of aerosol–cloud interactions (Charlson et al., 2007; Koren et al., 2007), the aerosol direct radiative effect, and Earth's energy budget (Eytan et al., 2025).

Our results also highlight measurement requirements for constraining aerosol variability and improving AOD retrievals in the CTZ. Active sensors such as LiDAR are particularly important because they provide the vertical information required to distinguish between aerosol variability occurring within the boundary layer, optically thin clouds, and aerosol removal or redistribution by cloud and precipitation processes. Column-integrated passive retrievals alone cannot always distinguish among these mechanisms. At the same time, the limited horizontal sampling of active sensors makes it difficult to determine the mesoscale context of an individual atmospheric profile. The combination of active profiling with satellite imagery is therefore particularly powerful: LiDAR provides detailed vertical information, while imagers provide the spectral and spatial context needed to relate each profile to the organization of the surrounding cloud field.

The present study is based on a limited number of cases from EUREC^{4}A and therefore provides hypotheses and a framework rather than a statistical characterization of the full range of CTZ conditions. Extending the D_{meso} framework to larger active–passive observational data sets and to large-eddy simulations would allow the relationships identified here to be tested systematically and would help separate the contributions of different processes to the observed mesoscale signal. A promising direction for improving aerosol retrievals in the CTZ is therefore to exploit large data sets of collocated active and passive observations. Combinations such as GOES–CALIPSO and MODIS–CALIPSO, as well as measurements from EarthCARE, could provide the statistics required to characterize systematically how aerosol and cloud properties vary with both cloud proximity and mesoscale cloud organization.

We suggest that mesoscale organization of the cloud field influences aerosol radiative properties through several pathways that include humidification, convective detrainment, precipitation removal and cloud processing, as well as through changes in the abundance of optically thin clouds and three-dimensional radiative effects. A deeper understanding of the interactions between mesoscale dynamics and the CTZ may yield new insights into aerosol–cloud–radiation interactions within the cloud field, and how they feed back onto the larger scales through local effects on the domain heating rates as well as the global energy budget. As an example, while prior work has focused on how the aerosol influences clouds through the aerosol *indirect effect*, we suggest a complementary perspective in which mesoscale dynamics and cloud organization shape the spatial distribution of aerosol

radiative properties, thereby modulating the aerosol *direct radiative effect*. Improved understanding of these multiscale interactions within the cloud field, spanning components from water vapor and aerosol to droplets and precipitation, may support the development of more unified, holistic frameworks for treating aerosol-cloud fields as a whole. Better representation of these processes in climate models offers the promise of reducing the persistent and large uncertainties that clouds and aerosol currently introduce into climate projections.

Conflict of Interest

The authors declare no conflicts of interest relevant to this study.

Availability Statement

GOES data is freely available at GOES-ABI (2026). The data can be downloaded by direct interaction with the Amazon Web Services S3 storage GOES-16 bucket ("s3://noaa-goes16/"). The WALES data, together with the data set used for the analysis, is found at Eytan (2026). The WALES data is a similar version to the data set found at EUREC4A (2020), with the addition of the retrievals of transmittance and extinction.

Acknowledgments
The authors thank Dr. Jan Kazil for insightful early discussions. This study was partly supported by NOAA's Climate Program Office Earth's Radiation Budget, Atmospheric Chemistry, Carbon Cycle, and Climate (AC4), and Climate Variability and Predictability (CVP) Programs, Grant NA23OAR4310294. E.E. was supported by the CIRES Visiting Fellows Program, funded by NOAA Cooperative Agreement NA22OAR4320151, and by the Next-gen award from the Institute for Environmental Sustainability at the Weizmann Institute of Science. S.G. has received funding from Horizon Europe programme under Grant Agreement No 101137680 via the project CERTAINTY (Cloud-aERosol inTeractions and their impActs IN The earth sYstem). The statements, findings, conclusions, and recommendations are those of the authors and do not necessarily reflect the views of NOAA or the U.S. Department of Commerce.

References

Ackerman, S. A., Holz, R. E., Frey, R., Eloranta, E. W., Maddux, B., & McGill, M. (2008). Cloud detection with modis. Part ii: Validation. *Journal of Atmospheric and Oceanic Technology*, *25*(7), 1073–1086. https://doi.org/10.1175/2007jtecha1053.1

Albright, A. L., Stevens, B., Bony, S., & Vogel, R. (2023). A new conceptual picture of the trade wind transition layer. *Journal of the Atmospheric Sciences*, *80*(6), 1547–1563. https://doi.org/10.1175/jas-d-22-0184.1

Anderson, T. L., Charlson, R. J., Winker, D. M., Ogren, J. A., & Holmén, K. (2003). Mesoscale variations of tropospheric aerosols. *Journal of the Atmospheric Sciences*, *60*(1), 119–136. https://doi.org/10.1175/1520-0469(2003)060<0119:mvota>2.0.co;2

Andreae, M. O. (2009). Correlation between cloud condensation nuclei concentration and aerosol optical thickness in remote and polluted regions. *Atmospheric Chemistry and Physics*, *9*(2), 543–556. https://doi.org/10.5194/acp-9-543-2009

Bar-Or, R., Altaratz, O., & Koren, I. (2011). Global analysis of cloud field coverage and radiative properties, using morphological methods and modis observations. *Atmospheric Chemistry and Physics*, *11*(1), 191–200. https://doi.org/10.5194/acp-11-191-2011

Bony, S., Lothon, M., Delanoë, J., Coutris, P., Etienne, J.-C., Aemisegger, F., et al. (2022). EUREC^{4}A observations from the SAFIRE ATR42 aircraft. *Earth System Science Data*, *14*(4), 2021–2064. https://doi.org/10.5194/essd-14-2021-2022

Bourgeois, Q., Ekman, A. M., Renard, J.-B., Krejci, R., Devasthale, A., Bender, F. A.-M., et al. (2018). How much of the global aerosol optical depth is found in the boundary layer and free troposphere? *Atmospheric Chemistry and Physics*, *18*(10), 7709–7720. https://doi.org/10.5194/acp-18-7709-2018

Bretherton, C., & Blossey, P. (2017). Understanding mesoscale aggregation of shallow cumulus convection using large-eddy simulation. *Journal of Advances in Modeling Earth Systems*, *9*(8), 2798–2821. https://doi.org/10.1002/2017ms000981

Chang, H., Hu, X., & Liu, Y. (2014). Calibrating modis aerosol optical depth for predicting daily pm2. 5 concentrations via statistical down-scaling. *Journal of Exposure Science and Environmental Epidemiology*, *24*(4), 398–404. https://doi.org/10.1038/jes.2013.90

Charlson, R. J., Ackerman, A. S., Bender, F. A.-M., Anderson, T. L., & Liu, Z. (2007). On the climate forcing consequences of the albedo continuum between cloudy and clear air. *Tellus B: Chemical and Physical Meteorology*, *59*(4), 715–727. https://doi.org/10.3402/tellusb.v59i4.17051

Christensen, M. W., Neubauer, D., Poulsen, C. A., Thomas, G. E., McGarragh, G. R., Povey, A. C., et al. (2017). Unveiling aerosol–cloud interactions–part 1: Cloud contamination in satellite products enhances the aerosol indirect forcing estimate. *Atmospheric Chemistry and Physics*, *17*(21), 13151–13164. https://doi.org/10.5194/acp-17-13151-2017

Conant, W. C., Nenes, A., & Seinfeld, J. H. (2002). Black carbon radiative heating effects on cloud microphysics and implications for the aerosol indirect effect 1. Extended köhler theory. *Journal of Geophysical Research*, *107*(D21), AAC–23. https://doi.org/10.1029/2002jd002094

Coutris, P., & Ehses, G. (2021). Safire atr42: Uhsas data, aeris [dataset]. https://doi.org/10.25326/220

Davison, J. L., Rauber, R. M., & Di Girolamo, L. (2013a). A revised conceptual model of the tropical marine boundary layer. Part ii: Detecting relative humidity layers using Bragg scattering from s-band radar. *Journal of the Atmospheric Sciences*, *70*(10), 3025–3046. https://doi.org/10.1175/jas-d-12-0322.1

Davison, J. L., Rauber, R. M., Di Girolamo, L., & LeMone, M. A. (2013b). A revised conceptual model of the tropical marine boundary layer. Part iii: Bragg scattering layer statistical properties. *Journal of the Atmospheric Sciences*, *70*(10), 3047–3062. https://doi.org/10.1175/jas-d-12-0323.1

Dror, T., Lehahn, Y., Altaratz, O., & Koren, I. (2018). Temporal-scale analysis of environmental controls on sea spray aerosol production over the south Pacific gyre. *Geophysical Research Letters*, *45*(16), 8637–8646. https://doi.org/10.1029/2018gl078707

Eck, T., Holben, B., Reid, J., Arola, A., Ferrare, R., Hostetler, C., et al. (2014). Observations of rapid aerosol optical depth enhancements in the vicinity of polluted cumulus clouds. *Atmospheric Chemistry and Physics*, *14*(21), 11633–11656. https://doi.org/10.5194/acp-14-11633-2014

EUREC4A. (2020). Eurec4a [dataset]. Retrieved from https://observations.ipsl.fr/aeris/eurec4a/#/

Eytan, E. (2026). Moisture aggregation and the cloud transition zone shape mesoscale aerosol properties [dataset]. https://csl.noaa.gov/groups/csl9/datasets/data/2026-Eytan/

Eytan, E., Gristey, J. J., & Feingold, G. (2025). The net radiative effect of the ill-defined clear-sky in the vicinity of clouds. *AGU Advances*, *6*(1), e2024AV001407. https://doi.org/10.1029/2024av001407

Eytan, E., Koren, I., Altaratz, O., Kostinski, A. B., & Ronen, A. (2020). Longwave radiative effect of the cloud twilight zone. *Nature Geoscience*, *13*(10), 669–673. https://doi.org/10.1038/s41561-020-0636-8

Feingold, G., Jiang, H., & Harrington, J. Y. (2005). On smoke suppression of clouds in Amazonia. *Geophysical Research Letters*, *32*(2). https://doi.org/10.1029/2004gl021369

21698996, 2026, 21, Downloaded from https://agupubs.onlinelibrary.wiley.com/doi/10.1029/2026JD047500 by Dtsch Zentrum F. Luft-U. Raum Fahrt In D. Helmholtz Gemein., Wiley Online Library on [11/11/2026]. See the Terms and Conditions (https://onlinelibrary.wiley.com/terms-and-conditions) on Wiley Online Library for rules of use; OA articles are governed by the applicable Creative Commons License

Garrigues, S., Ades, M., Remy, S., Flemming, J., Kipling, Z., Laszlo, I., et al. (2023). Impact of assimilating noaa viirs aerosol optical depth (aod) observations on global aod analysis from the copernicus atmosphere monitoring service (cams). *Atmospheric Chemistry and Physics*, *23*(18), 10473–10487. https://doi.org/10.5194/acp-23-10473-2023

George, G., Stevens, B., Bony, S., Vogel, R., & Naumann, A. K. (2023). Widespread shallow mesoscale circulations observed in the trades. *Nature Geoscience*, *16*(7), 584–589. https://doi.org/10.1038/s41561-023-01215-1

GOES-ABI. (2026). Goes-abi [dataset]. Retrieved from https://registry.opendata.aws/noaa-goes/

Graßl, H. (1975). Albedo reduction and radiative heating of clouds by absorbing aerosol particles. *Beiträge zur Physik der Atmosphäre*, *48*, 199–210.

Groß, S., Esselborn, M., Weinzierl, B., Wirth, M., Fix, A., & Petzold, A. (2013). Aerosol classification by airborne high spectral resolution LiDAR observations. *Atmospheric Chemistry and Physics*, *13*(5), 2487–2505.

Groß, S., Tesche, M., Freudenthaler, V., Toledano, C., Wiegner, M., Ansmann, A., & Seefeldner, M. (2011). Characterization of Saharan dust, marine aerosols and mixtures of biomass-burning aerosols and dust by means of multi-wavelength depolarization and raman LiDAR measurements during samum 2. *Tellus B: Chemical and Physical Meteorology*, *63*(4), 706–724.

Gutleben, M., Groß, S., Heske, C., & Wirth, M. (2022). Wintertime Saharan dust transport towards the caribbean: An airborne LiDAR case study during eurec 4 a. *Atmospheric Chemistry and Physics*, *22*(11), 7319–7330. https://doi.org/10.5194/acp-22-7319-2022

Gutleben, M., Groß, S., & Wirth, M. (2019). Cloud macro-physical properties in saharan-dust-laden and dust-free north atlantic trade wind regimes: A LiDAR case study. *Atmospheric Chemistry and Physics*, *19*(16), 10659–10673. https://doi.org/10.5194/acp-19-10659-2019

Gutleben, M., Groß, S., Wirth, M., & Mayer, B. (2020). Radiative effects of long-range-transported Saharan air layers as determined from airborne LiDAR measurements. *Atmospheric Chemistry and Physics*, *20*(20), 12313–12327. https://doi.org/10.5194/acp-20-12313-2020

Haarig, M., Ansmann, A., Baars, H., Jimenez, C., Veselovskii, I., Engelmann, R., & Althausen, D. (2018). Depolarization and LiDAR ratios at 355, 532, and 1064 nm and microphysical properties of aged tropospheric and stratospheric Canadian wildfire smoke. *Atmospheric Chemistry and Physics*, *18*(16), 11847–11861. https://doi.org/10.5194/acp-18-11847-2018

Haslett, S. L., Taylor, J. W., Deetz, K., Vogel, B., Babić, K., Kalthoff, N., et al. (2019). The radiative impact of out-of-cloud aerosol hygroscopic growth during the summer monsoon in southern west Africa. *Atmospheric Chemistry and Physics*, *19*(3), 1505–1520. https://doi.org/10.5194/acp-19-1505-2019

Heidinger, A. (2011a). Algorithm theoretical basis document abi cloud height. *NOAA NESDIS Center for Satellite Applications and Research*. http://www.goes-r.gov/products/ATBDs/baseline/Cloud_CldHeight_v2.0_no_color.pdf

Heidinger, A. (2011b). *Algorithm theoretical basis document: Abi cloud mask*. University of Wisconsin.

Heidinger, A., Pavolonis, M. J., Calvert, C., Hoffman, J., Nebuda, S., Straka III, W., et al. (2020). Abi cloud products from the goes-r series. In *The goes-r series* (pp. 43–62). Elsevier.

Hirsch, E., Koren, I., Levin, Z., Altaratz, O., & Agassi, E. (2014). On transition-zone water clouds. *Atmospheric Chemistry and Physics*, *14*(17), 9001–9012. https://doi.org/10.5194/acp-14-9001-2014

Hu, R., Li, Z., & Su, T. (2025). Investigating aerosol hygroscopicity in the subcloud transition zone and at the surface in the southern Great Plains. *Journal of Geophysical Research: Atmospheres*, *130*(17), e2024JD041925. https://doi.org/10.1029/2024jd041925

Jahani, B., Andersen, H., Calbó, J., González, J.-A., & Cermak, J. (2022). Longwave radiative effect of the cloud–aerosol transition zone based on ceres observations. *Atmospheric Chemistry and Physics*, *22*(2), 1483–1494. https://doi.org/10.5194/acp-22-1483-2022

Janssens, M., De Arellano, J. V.-g., Van Heerwaarden, C. C., De Roode, S. R., Siebesma, A. P., & Glassmeier, F. (2023). Nonprecipitating shallow cumulus convection is intrinsically unstable to length scale growth. *Journal of the Atmospheric Sciences*, *80*(3), 849–870. https://doi.org/10.1175/jas-d-22-0111.1

Janssens, M., Vilŕ-Guerau de Arellano, J., Scheffer, M., Antonissen, C., Siebesma, A. P., & Glassmeier, F. (2021). Cloud patterns in the trades have four interpretable dimensions. *Geophysical Research Letters*, *48*(5), e2020GL091001. https://doi.org/10.1029/2020gl091001

Jiménez, P. A. (2020). Assessment of the goes-16 clear sky mask product over the contiguous USA using calipso retrievals. *Remote Sensing*, *12*(10), 1630. https://doi.org/10.3390/rs12101630

John, V. O., Holl, G., Allan, R. P., Buehler, S. A., Parker, D. E., & Soden, B. J. (2011). Clear-sky biases in satellite infrared estimates of upper tropospheric humidity and its trends. *Journal of Geophysical Research*, *116*(D14), D14108. https://doi.org/10.1029/2010jd015355

Konow, H., Ewald, F., George, G., Jacob, M., Klingebiel, M., Kölling, T., et al. (2021). Eurec^{4}a's halo. *Earth System Science Data*, *13*(12), 5545–5563. https://doi.org/10.5194/essd-13-5545-2021

Koren, I., Feingold, G., & Remer, L. A. (2010). The invigoration of deep convective clouds over the Atlantic: Aerosol effect, meteorology or retrieval artifact? *Atmospheric Chemistry and Physics*, *10*(18), 8855–8872. https://doi.org/10.5194/acp-10-8855-2010

Koren, I., Kaufman, Y. J., Remer, L. A., & Martins, J. V. (2004). Measurement of the effect of Amazon smoke on inhibition of cloud formation. *Science*, *303*(5662), 1342–1345. https://doi.org/10.1126/science.1089424

Koren, I., Oreopoulos, L., Feingold, G., Remer, L., & Altaratz, O. (2008). How small is a small cloud? *Atmospheric Chemistry and Physics*, *8*(14), 3855–3864. https://doi.org/10.5194/acp-8-3855-2008

Koren, I., Remer, L. A., Kaufman, Y. J., Rudich, Y., & Martins, J. V. (2007). On the twilight zone between clouds and aerosols. *Geophysical Research Letters*, *34*(8). https://doi.org/10.1029/2007gl029253

Laszlo, I., Ciren, P., Liu, H., Kondragunta, S., Tarpley, J. D., & Goldberg, M. D. (2008). Remote sensing of aerosol and radiation from geostationary satellites. *Advances in Space Research*, *41*(11), 1882–1893. https://doi.org/10.1016/j.asr.2007.06.047

Leahy, L., Wood, R., Charlson, R., Hostetler, C., Rogers, R., Vaughan, M., & Winker, D. (2012). On the nature and extent of optically thin marine low clouds. *Journal of Geophysical Research*, *117*(D22). https://doi.org/10.1029/2012jd017929

Lee, H. J. (2020). Advancing exposure assessment of pm2. 5 using satellite remote sensing: A review. *Asian Journal of Atmospheric Environment*, *14*(4), 319–334. https://doi.org/10.5572/ajae.2020.14.4.319

Levy, R. C., Mattoo, S., Munchak, L., Remer, L., Sayer, A., Patadia, F., & Hsu, N. (2013). The collection 6 modis aerosol products over land and ocean. *Atmospheric Measurement Techniques*, *6*(11), 2989–3034. https://doi.org/10.5194/amt-6-2989-2013

Liang, J., & Griswold, J. D. S. (2025). Assessment of aerosol optical depth, cloud fraction, and liquid water path in cmip6 models using satellite observations. *Remote Sensing*, *17*(14), 2439. https://doi.org/10.3390/rs17142439

Loeb, N. G., & Manalo-Smith, N. (2005). Top-of-atmosphere direct radiative effect of aerosols over global oceans from merged ceres and modis observations. *Journal of Climate*, *18*(17), 3506–3526. https://doi.org/10.1175/jcli3504.1

Ma, X., & Yu, F. (2015). Seasonal and spatial variations of global aerosol optical depth: Multi-year modelling with geos-chem-apm and comparisons with multiple-platform observations. *Tellus B: Chemical and Physical Meteorology*, *67*(1), 25115. https://doi.org/10.3402/tellusb.v67.25115

Marshak, A., Ackerman, A., da Silva, A., Eck, T., Holben, B., Kahn, R., et al. (2021). Aerosol properties in cloudy environments from remote sensing observations: A review of the current state of knowledge. *Bulletin of the American Meteorological Society*, *102*(11), E2177–E2197. https://doi.org/10.1175/bams-d-20-0225.1

21698996, 2026, 21, Downloaded from https://agupubs.onlinelibrary.wiley.com/doi/10.1029/2026JD047500 by Dtsch Zentrum F. Luft-U. Raum Fahrt In D. Helmholtz Gemein., Wiley Online Library on [11/11/2026]. See the Terms and Conditions (https://onlinelibrary.wiley.com/terms-and-conditions) on Wiley Online Library for rules of use; OA articles are governed by the applicable Creative Commons License

McCoy, I. L., McCoy, D. T., Wood, R., Zuidema, P., & Bender, F. A.-M. (2023). The role of mesoscale cloud morphology in the shortwave cloud feedback. *Geophysical Research Letters*, *50*(2), e2022GL101042. https://doi.org/10.1029/2022gl101042

Mieslinger, T., Stevens, B., Kölling, T., Brath, M., Wirth, M., & Buehler, S. A. (2022). Optically thin clouds in the trades. *Atmospheric Chemistry and Physics*, *22*(10), 6879–6898. https://doi.org/10.5194/acp-22-6879-2022

Narenpitak, P., Kazil, J., Yamaguchi, T., Quinn, P., & Feingold, G. (2021). From sugar to flowers: A transition of shallow cumulus organization during atomic. *Journal of Advances in Modeling Earth Systems*, *13*(10), e2021MS002619. https://doi.org/10.1029/2021ms002619

NOAA GOES-R Algorithm Working Group, and GOES-R Program Office. (2018). *NOAA GOES-R Series Advanced Baseline Imager (ABI) level 2 Cloud Optical Depth (COD) (Tech. Rep.)*. NOAA National Centers for Environmental Information (NCEI). https://doi.org/10.7289/V58G8J02

Orlanski, I. (1975). A rational subdivision of scales for atmospheric processes. *Bulletin of the American Meteorological Society*, 527–530.

Randles, C., Da Silva, A., Buchard, V., Colarco, P., Darmenov, A., Govindaraju, R., et al. (2017). The merra-2 aerosol reanalysis, 1980 onward. Part I: System description and data assimilation evaluation. *Journal of Climate*, *30*(17), 6823–6850. https://doi.org/10.1175/jcli-d-16-0609.1

Rixen, M., Windmiller, J., & Stevens, B. (2025). Influence of mesoscale organization on the formation of humidity haloes. *Geophysical Research Letters*, *52*(22), e2025GL119013. https://doi.org/10.1029/2025gl119013

Rodts, S. M., Duynkerke, P. G., & Jonker, H. J. (2003). Size distributions and dynamical properties of shallow cumulus clouds from aircraft observations and satellite data. *Journal of the Atmospheric Sciences*, *60*(16), 1895–1912. https://doi.org/10.1175/1520-0469(2003)060<1895:sdadpo>2.0.co;2

Ruiz de Morales, J., Calbó, J., González, J.-A., Andersen, H., Cermak, J., Fuchs, J., & Sola, Y. (2026). Global assessment of the cloud-aerosol transition zone using calipso. *Advances in Atmospheric Sciences*, *43*(2), 321–335. https://doi.org/10.1007/s00376-025-5052-y

Schmit, T. J., Gunshor, M. M., Menzel, W. P., Gurka, J. J., Li, J., & Bachmeier, A. S. (2005). Introducing the next-generation advanced baseline imager on goes-r. *Bulletin of the American Meteorological Society*, *86*(8), 1079–1096. https://doi.org/10.1175/bams-86-8-1079

Schotland, R. M., Sassen, K., & Stone, R. (1971). Observations by LiDAR of linear depolarization ratios for hydrometeors. *Journal of Applied Meteorology and Climatology*, *10*(5), 1011–1017. https://doi.org/10.1175/1520-0450(1971)010<1011:oblold>2.0.co;2

Schwarz, K., Cermak, J., Fuchs, J., & Andersen, H. (2017). Mapping the twilight zone—what we are missing between clouds and aerosols. *Remote Sensing*, *9*(6), 577. https://doi.org/10.3390/rs9060577

Seinfeld, J. H., Bretherton, C., Carslaw, K. S., Coe, H., DeMott, P. J., Dunlea, E. J., et al. (2016). Improving our fundamental understanding of the role of aerosol-cloud interactions in the climate system. *Proceedings of the National Academy of Sciences*, *113*(21), 5781–5790. https://doi.org/10.1073/pnas.1514043113

Sellegri, K., Simo, R., Wang, B., Alpert, P. A., Altieri, K., Burrows, S., et al. (2024). Influence of open ocean biogeochemistry on aerosol and clouds: Recent findings and perspectives. *Elementa: Science of the Anthropocene*, *12*(1), 00058. https://doi.org/10.1525/elementa.2023.00058

Stevens, B., Bony, S., Farrell, D., Ament, F., Blyth, A., Fairall, C., et al. (2021). Eurec 4 a. *Earth System Science Data*, *13*(8), 4067–4119. https://doi.org/10.5194/essd-13-4067-2021

Su, W., Loeb, N. G., Schuster, G. L., Chin, M., & Rose, F. G. (2013). Global all-sky shortwave direct radiative forcing of anthropogenic aerosols from combined satellite observations and gocart simulations. *Journal of Geophysical Research: Atmospheres*, *118*(2), 655–669. https://doi.org/10.1029/2012jd018294

Thorsen, T. J., Ferrare, R. A., Kato, S., & Winker, D. M. (2020). Aerosol direct radiative effect sensitivity analysis. *Journal of Climate*, *33*(14), 6119–6139. https://doi.org/10.1175/jcli-d-19-0669.1

Tompkins, A. M. (2001). Organization of tropical convection in low vertical wind shears: The role of water vapor. *Journal of the Atmospheric Sciences*, *58*(6), 529–545. https://doi.org/10.1175/1520-0469(2001)058<0529:ootcil>2.0.co;2

Twohy, C. H., Coakley Jr., J. A., & Tahnk, W. R. (2009). Effect of changes in relative humidity on aerosol scattering near clouds. *Journal of Geophysical Research*, *114*(D5). https://doi.org/10.1029/2008jd010991

Várnai, T., & Marshak, A. (2009). Modis observations of enhanced clear sky reflectance near clouds. *Geophysical Research Letters*, *36*(6). https://doi.org/10.1029/2008gl037089

Várnai, T., & Marshak, A. (2014). Near-cloud aerosol properties from the 1 km resolution modis ocean product. *Journal of Geophysical Research: Atmospheres*, *119*(3), 1546–1554. https://doi.org/10.1002/2013jd020633

Várnai, T., & Marshak, A. (2018). Satellite observations of cloud-related variations in aerosol properties. *Atmosphere*, *9*(11), 430. https://doi.org/10.3390/atmos9110430

Wen, G., Marshak, A., & Cahalan, R. F. (2006). Impact of 3-d clouds on clear-sky reflectance and aerosol retrieval in a biomass burning region of Brazil. *IEEE Geoscience and Remote Sensing Letters*, *3*(1), 169–172. https://doi.org/10.1109/lgrs.2005.861386

Wen, G., Marshak, A., Remer, L., Levy, R., Loeb, N., Várnai, T., & Cahalan, R. F. (2013). Correction of modis aerosol retrieval for 3d radiative effects in broken cloud fields. *AIP Conference Proceedings*, *1531*, 280–283.

Wirth, M. (2021). Cloud top height derived from airborne measurements with the wales LiDAR during the eurec4a field campaign [dataset]. *aeris*. https://doi.org/10.25326/216

Wirth, M., Fix, A., Mahnke, P., Schwarzer, H., Schrandt, F., & Ehret, G. (2009). The airborne multi-wavelength water vapor differential absorption LiDAR wales: System design and performance. *Applied Physics B*, *96*(1), 201–213. https://doi.org/10.1007/s00340-009-3365-7

Wood, R., Kuan-Ting, O., Bretherton, C. S., Mohrmann, J., Albrecht, B. A., Zuidema, P., et al. (2018). Ultraclean layers and optically thin clouds in the stratocumulus-to-cumulus transition. Part i: Observations. *Journal of the Atmospheric Sciences*, *75*(5), 1631–1652. https://doi.org/10.1175/jas-d-17-0213.1

Wood, R., & Tseng, H.-H. (2018). Deeper, precipitating pbls associated with optically thin veil clouds in the sc-cu transition. *Geophysical Research Letters*, *45*(10), https://doi.org/10.1029/2018GL077084

Yang, C. K., Chiu, J. C., Marshak, A., Feingold, G., Várnai, T., Wen, G., et al. (2022). Near-cloud aerosol retrieval using machine learning techniques, and implied direct radiative effects. *Geophysical Research Letters*, *49*(20), e2022GL098274. https://doi.org/10.1029/2022gl098274

Yu, H., Kaufman, Y., Chin, M., Feingold, G., Remer, L., Anderson, T., et al. (2006). A review of measurement-based assessments of the aerosol direct radiative effect and forcing. *Atmospheric Chemistry and Physics*, *6*(3), 613–666. https://doi.org/10.5194/acp-6-613-2006

Zhai, S., Jacob, D. J., Brewer, J. F., Li, K., Moch, J. M., Kim, J., et al. (2021). Relating geostationary satellite measurements of aerosol optical depth (aod) over east Asia to fine particulate matter (pm 2.5): Insights from the korus-aq aircraft campaign and geos-chem model simulations. *Atmospheric Chemistry and Physics*, *21*(22), 16775–16791. https://doi.org/10.5194/acp-21-16775-2021

References From the Supporting Information

Klett, J. D. (1985). Lidar inversion with variable backscatter/extinction ratios. *Applied Optics*, *24*(11), 1638–1643. https://doi.org/10.1364/ao.24.001638

21698996, 2026, 21, Downloaded from https://agupubs.onlinelibrary.wiley.com/doi/10.1029/2026JD047500 by Dtsch Zentrum F. Luft-U. Raum Fahrt In D. Helmholtz Gemein., Wiley Online Library on [11/11/2026]. See the Terms and Conditions (https://onlinelibrary.wiley.com/terms-and-conditions) on Wiley Online Library for rules of use; OA articles are governed by the applicable Creative Commons License